The Astrophysical Journal, 831:145 (20pp), 2016 November 10 doi:10.3847/0004-637X/831/2/145

LONG-TERM X-RAY VARIABILITY OF TYPICAL ACTIVE GALACTIC NUCLEI IN THE DISTANT UNIVERSE

G. Yang[1,2], W. N. Brandt[1,2,3], B. Luo[1,4], Y. Q. Xue[5], F. E. Bauer[6,7,8,9], M. Y. Sun[1,5,10], S. Kim[6], S. Schulze[6,7], X. C. Zheng[5], M. Paolillo[11,12], O. Shemmer[13], T. Liu[5], D. P. Schneider[1,2], C. Vignali[14], F. Vito[1,2], and J.-X. Wang[5]
[1] Department of Astronomy and Astrophysics, 525 Davey Lab, Pennsylvania State University, University Park, PA 16802, USA; gxy909@psu.edu
[2] Institute for Gravitation and the Cosmos, Pennsylvania State University, University Park, PA 16802, USA
[3] Department of Physics, 104 Davey Laboratory, Pennsylvania State University, University Park, PA 16802, USA
[4] School of Astronomy & Space Science, Nanjing University, Nanjing 210093, China
[5] CAS Key Laboratory for Research in Galaxies and Cosmology, Center for Astrophysics, Department of Astronomy, University of Science and Technology of China, Chinese Academy of Sciences, Hefei, Anhui 230026, China
[6] Instituto de Astrofísica, Facultad de Física, Pontificia Universidad Católica de Chile, Casilla 306, Santiago 22, Chile
[7] Millennium Institute of Astrophysics, Nuncio Monseñor Sótero Sanz 100, Providencia, Santiago, Chile
[8] Space Science Institute, 4750 Walnut Street, Suite 205, Boulder, CO 80301, USA
[9] EMBIGGEN Anillo, Concepción, Chile
[10] Department of Astronomy and Institute of Theoretical Physics and Astrophysics, Xiamen University, Xiamen, Fujian 361005, China
[11] Dipartimento di Fisica, Universita Federico II, Napoli I-80126, Italy
[12] ASI Science Data Center, via del Politecnico snc, Roma I-80126, Italy
[13] Department of Physics, University of North Texas, Denton, TX 76203, USA
[14] Universita di Bologná, Via Ranzani 1, Bologna, Italy
Received 2016 April 17; revised 2016 August 26; accepted 2016 August 27; published 2016 November 3

ABSTRACT

We perform long-term (≈15 years, observed-frame) X-ray variability analyses of the 68 brightest radio-quiet active galactic nuclei (AGNs) in the 6 Ms *Chandra* Deep Field-South survey; the majority are in the redshift range of 0.6–3.1, providing access to penetrating rest-frame X-rays up to ≈10–30 keV. Of the 68 sources, 24 are optical spectral type I AGNs, and the rest (44) are type II AGNs. The timescales probed in this work are among the longest for X-ray variability studies of distant AGNs. Photometric analyses reveal widespread photon flux variability: 90% of AGNs are variable above a 95% confidence level, including many X-ray obscured AGNs and several optically classified type II quasars. We characterize the intrinsic X-ray luminosity (L_X) and absorption (N_H) variability via spectral fitting. Most (74%) sources show L_X variability; the variability amplitudes are generally smaller for quasars. A Compton-thick candidate AGN shows variability of its high-energy X-ray flux, indicating the size of reflecting material to be $\lesssim$0.3 pc. L_X variability is also detected in a broad absorption line quasar. The N_H variability amplitude for our sample appears to rise as time separation increases. About 16% of sources show N_H variability. One source transitions from an X-ray unobscured to obscured state, while its optical classification remains type I; this behavior indicates the X-ray eclipsing material is not large enough to obscure the whole broad-line region.

Key words: galaxies: active – galaxies: nuclei – methods: data analysis – quasars: general – X-rays: galaxies – X-rays: general

Supporting material: machine-readable table

1. INTRODUCTION

Variability studies are valuable for probing the physical properties of active galactic nuclei (AGNs) (e.g., Ulrich et al. 1997; Peterson 2001). Simple light-travel time arguments enable a first-order estimation of the sizes of the radiation-emitting regions. More detailed reverberation-based studies provide size estimates of different components, e.g., the correlations among multi-color light curves give the temperature profiles of accretion disks (e.g., Fausnaugh et al. 2015), time lags between the continuum and emission lines indicate the radius of the broad-line region (BLR) (e.g., Peterson 2014), and delays of the near-infrared dust emission compared to the optical disk emission constrain the inner size of the dusty torus (e.g., Koshida et al. 2014). Changes in absorption provide insights into the absorbing matter, e.g., the variability of broad absorption line (BAL) troughs reveals wind properties (e.g., Filiz Ak et al. 2013), and variations of optical reddening and X-ray absorption indicate a clumpy nature of the ambient gas (e.g., Goodrich 1995; Netzer 2015). In AGN jet studies, the rapid variability of blazars' γ-ray emission often indicates small emitting regions and a relativistically beamed nature of the radiation (e.g., Begelman et al. 2008; Abdo et al. 2010).

X-ray variability is of great importance among AGN variability studies. In AGN spectral energy distributions (SEDs), luminous X-ray emission is almost universal and often a significant contributor to the total source power (e.g., Gibson et al. 2008). X-ray variability is generally of larger amplitude and more rapid compared to that at longer wavelengths (e.g., Ulrich et al. 1997; Peterson 2001), indicating that the high-energy radiation is probing the immediate vicinity of the supermassive black hole (SMBH). For the majority of the population of obscured AGNs, the penetrating nature of X-rays often allows variability studies of emission as well as absorption (e.g., Puccetti et al. 2014; Hernández-García et al. 2015).

Intensive X-ray variability analyses have been performed for the radio-quiet AGNs that are the majority population. Studies of broadband X-ray continuum variability have found that local Seyfert 1s (i.e., unabsorbed AGNs) are highly X-ray variable, and that the variation amplitude generally decreases as luminosity increases (e.g., Nandra et al. 1997; Ponti

et al. 2012). This amplitude-luminosity relation might be a byproduct of a primary amplitude–SMBH mass relation (e.g., Ponti et al. 2012 and references therein). Seyfert 2s, especially Compton-thick (obscuration column density $N_{\rm H} \gtrsim 1.5 \times 10^{24}\,{\rm cm}^{-2}$) ones, tend to be less X-ray variable than Seyfert 1s at least on timescales of hours or less (e.g., Turner et al. 1997; Awaki et al. 2006; Hernández-García et al. 2015). Studies of distant AGNs, such as optically selected quasars, have also reported prevalent X-ray variability (e.g., Gibson & Brandt 2012, G12 hereafter; Shemmer et al. 2014) and a similar amplitude–luminosity relation as seen in local Seyfert galaxies (e.g., Almaini et al. 2000; Paolillo et al. 2004; Papadakis et al. 2008; Lanzuisi et al. 2014). Compared to the X-ray continuum, the narrow Fe K emission-line components are less variable (e.g., Markowitz et al. 2003), consistent with the picture that they originate from the outer disk or torus. Recent works (e.g., Zoghbi et al. 2012; Kara et al. 2013) reveal short-timescale (minutes) lags of the broad Fe K emission-line components relative to the continuum, suggesting they are emitted from the inner disk illuminated by the continuum X-rays. X-ray photoelectric absorption variability has also been found in many Seyfert 2s (e.g., Risaliti et al. 2002, 2007). Modeling of the observed absorption variations suggests this absorption originates in gas clouds in the BLR or torus orbiting the central source (e.g., Maiolino et al. 2010; Markowitz et al. 2014; Torricelli-Ciamponi et al. 2014; Netzer 2015). X-ray absorption variability has also been widely investigated in warm absorbers, BAL quasar winds, and ultra fast outflows (UFOs), usefully characterizing wind properties (e.g., Chartas et al. 2009; Matt et al. 2011; Saez et al. 2012; King & Pounds 2015; Scott et al. 2015).

The X-ray variability of AGNs generally shows a red-noise power spectral density (PSD, e.g., Uttley et al. 2002); i.e., AGNs vary by larger amplitudes on longer timescales. X-ray variability analyses on longer timescales thus have a better chance of detecting variability in data of a given signal-to-noise ratio (S/N), thereby providing physical insights about the nature of the AGNs. Long-term variability studies are also helpful in evaluating the effects of AGN variability upon statistical inferences made about source populations in single-epoch X-ray surveys. Furthermore, long-term X-ray variability studies might capture novel AGN phenomena; e.g., "changing look" events (e.g., Matt et al. 2003; Ricci et al. 2016), emission state changes (e.g., Miniutti et al. 2012), and torus eclipse events (e.g., Markowitz et al. 2014). Variability analyses on timescales of years can probe the regime of mechanical instabilities of the accretion disk (assuming a $\sim 10^8\,M_\odot$ SMBH; see, e.g., Peterson 2001).

Motivated by the importance of X-ray variability studies, especially on long timescales, we here explore the X-ray variability of the X-ray brightest radio-quiet AGNs in the *Chandra* Deep Field-South (CDF-S; e.g., Xue et al. 2011; B. Luo et al. 2016, in preparation, L16 hereafter). We take advantage of the data products from the observations by *Chandra* of the CDF-S. The observations span ≈15 years and are well separated, enabling us to characterize long-term variability properties of distant AGNs. The rest-frame timescales probed in this study are among the longest for X-ray variability studies of distant AGNs (see Figure 1), and they are the longest for an X-ray selected AGN sample. Table 1 summarizes the basic sample properties in this work and previous variability studies of distant AGNs. Furthermore, the long exposure times, low source-cell backgrounds, and state-of-the-art source-extraction techniques (Xue et al. 2011, 2016; L16) yield high-quality data products, allowing us to perform, in addition to photometric analyses, reliable basic spectral analyses. We assess variability of both intrinsic (absorption-corrected) X-ray luminosity and absorption, and study their dependence on timescale and source properties.

The paper is structured as follows. We describe the observations, data reduction, and sample selection in Section 2. In Section 3, we perform both photometric and spectral variability analyses and investigate variability dependences on source properties and timescales. We discuss our results and draw conclusions in Section 4.

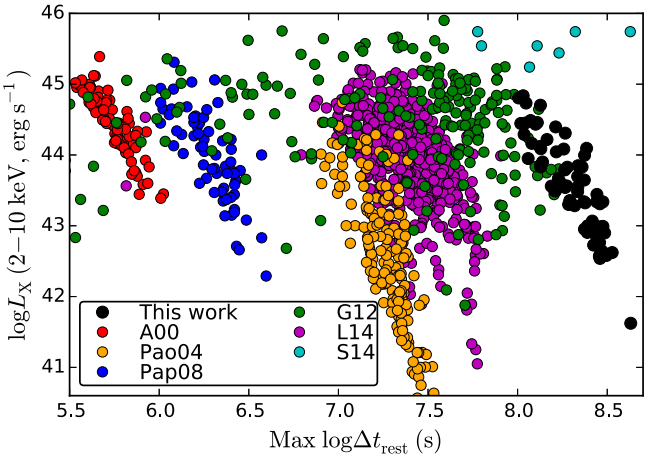

Figure 1. X-ray luminosity as a function of maximum rest-frame time span. Different colors indicate samples from different studies (A00: Almaini et al. 2000; Pao04: Paolillo et al. 2004; Pap08: Papadakis et al. 2008; G12: Gibson & Brandt 2012, L14: Lanzuisi et al. 2014; S14: Shemmer et al. 2014). The X-ray luminosities from the literature are derived assuming a power-law photon index of 1.8. The X-ray luminosities of our sources are the mean values detailed in Section 3.2.1. The maximum rest-frame time spans for A00, Pao04, and Pap08 are calculated assuming that each source is present in all observations; this assumption might overestimate time spans for some sources. The rest-frame time spans probed in this work are among the longest for X-ray variability studies.

Table 1
Summary of Variability Studies of Distant AGNs

Reference	Med. Max. $\log\Delta t_{\rm rest}$	Med. Counts	z	$\log L_{\rm X}$	N
(1)	(2)	(3)	(4)	(5)	(6)
This work	8.3	1399	0.6–3.1	42.7–44.5	68
A00	5.7	63	0.6–2.0	43.8–45.0	86
Pao04	7.3	64	0.3–2.1	41.0–43.9	186
Pap08	6.3	280	0.6–2.7	43.1–44.7	66
G12	7.3	130	0.4–3.0	43.6–45.2	264
L14	7.4	350	0.5–2.3	43.2–44.7	638
S14	8.1	···	1.8–4.3	45.4–45.7	7

Note. (1) A00: Almaini et al. (2000); Pao04: Paolillo et al. (2004); Pap08: Papadakis et al. (2008); G12: Gibson & Brandt (2012), L14: Lanzuisi et al. (2014); S14: Shemmer et al. (2014). For Pao04, we only include sources with redshift information. (2) Sample median of maximum rest-frame time spans, where $\Delta t_{\rm rest}$ is in units of seconds. (3) Sample median of net counts. We do not calculate the median counts of S14 due to large fluctuations in counts among their seven sources. (4) Redshift range. We adopt the 10th–90th percentile ranges. (5) X-ray luminosity range (10th–90th percentile). (6) Number of sources.

Table 2
Observation Binning

Epoch	Start Date	End Date	Bin Width (yr)	Exp.[a] (Ms)	Obs.[b]
1	1999 Oct	2000 Dec	1.19	0.94	11
2	2007 Sep	2007 Nov	0.12	0.97	12
3	2010 Mar	2010 Jul	0.34	1.98	31
4	2014 Jun	2015 Jan	0.57	1.85	30

Notes.
[a] Total exposure time of observations in each bin.
[b] Number of observations in each bin.

Throughout this paper, we assume a cosmology with $H_0 = 70$ km s^{-1} Mpc^{-1}, $\Omega_M = 0.3$, and $\Omega_\Lambda = 0.7$. We adopt $N_{\rm H} = 8.8 \times 10^{19}$ cm^{-2} as the value of the column density of Galactic absorption (Stark et al. 1992). Quoted uncertainties are at the 1σ (68%) confidence level, unless otherwise stated. We adopt the standard naming convention for *Chandra* CDF-S sources, i.e., "CXOCDFS J033XXX.X–27XXXX"; for simplicity, we drop the "CXOCDFS" and quote as "J033XXX.X–27XXXX" directly.

2. DATA AND SAMPLE

2.1. Observations and Data Reduction

This work is based on the *Chandra* CDF-S data. The observations were taken from 1999 October to 2015 January with a total observation time of 5.7 Ms (referred as 6 Ms, hereafter). In total, there are 84 observations utilized with median exposure time ≈60 ks. All of the 84 observations were performed using the Advanced CCD Imaging Spectrometer imaging array (ACIS-I; Garmire et al. 2003; see L16 for more observation details). The data products were processed from level 1 files (L16) using CIAO v4.7 with CALDB v4.6.7. Spectra and photometry from each observation were extracted using ACIS Extract v4864 (AE; Broos et al. 2010). For each source, AE constructs observation-specific polygonal extraction apertures. The apertures are chosen to maximize S/N, based on simulations of point spread functions (PSFs).

Since most CDF-S sources have low S/N in single observations, we bin data from neighboring observations as one "epoch" to enhance the S/N. We have binned the observations so that each epoch consists of observations totaling about 1–2 Ms of exposure time, resulting in a photometric/spectral set of four epochs for each source. Our bins were chosen to include as much data as possible in the shortest possible span of time, in order to minimize variability effects within the bins. The bin widths range from about several months to one year. Due to cosmological time dilation, the rest-frame total time span and bin width are a factor of $1 + z$ shorter than the observed-frame values. Table 2 shows our observation binning approach. This binning process is carried out using the MERGE_OBSERVATIONS stage of AE. We do not include *XMM-Newton* CDF-S data in our analyses, since cross-calibration between *Chandra* and *XMM-Newton* spectra can be problematic (e.g., Iwasawa et al. 2015), and the *XMM-Newton* data have substantially higher background. Also, most of the *XMM-Newton* observations (∼85% of the exposure time) were taken within about 1.5 years (Ranalli et al. 2013) and thus are not suitable for year-scale variability studies.

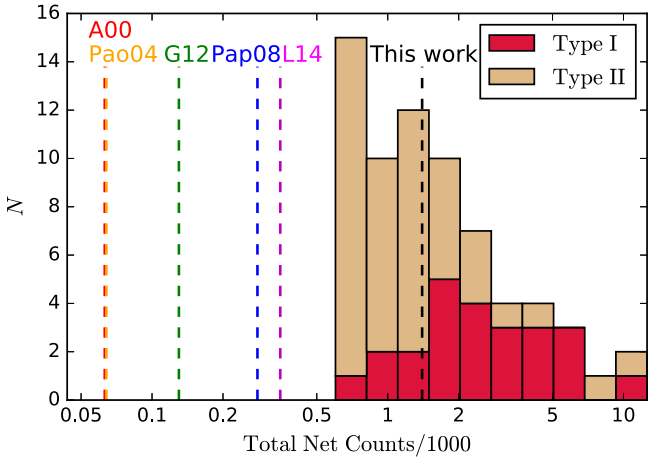

Figure 2. Histogram of total net counts of our 68 sources. The red and brown bars indicate type I and type II AGNs. The vertical dashed lines indicate the median counts of this work and previous studies, respectively (A00: Almaini et al. 2000; Pao04: Paolillo et al. 2004; Pap08: Papadakis et al. 2008; G12: Gibson & Brandt 2012, L14: Lanzuisi et al. 2014). Note that A00 and Pao04 have very similar median counts. We do not show the median counts of Shemmer et al. (2014) due to large fluctuations in counts among their seven sources. Our sample only includes bright sources with counts greater than 600. Our type I AGNs generally have more available counts than their type II counterparts.

2.2. Sample Selection

To perform reliable analyses, we select our sources based on the following criteria:

1. Classified as an AGN in the L16 catalog,
2. Not identified as a radio-loud AGN by Bonzini et al. (2013),
3. More than 600 total net counts (i.e., background subtracted, 0.5–7 keV) in the full 6 Ms exposure, and
4. Off-axis angle $<8'$.

The first criterion classifies AGNs based upon the X-ray luminosity, X-ray spectral shape, X-ray-to-optical flux ratio, X-ray-to-radio luminosity ratio, and optical emission line properties, and it is described in more detail in Section 4.4 of Xue et al. (2011). The second criterion excludes the sources possibly affected by jet-linked emission in their X-ray spectra, to avoid dealing with the significant additional complexity of such emission (see, e.g., Miller et al. 2011). This criterion removes only six sources that satisfy the other three criteria. The third constraint guarantees suitable photon statistics for variability characterization and spectral fitting; given the observed X-ray variability of our sources, we do not have any problematic cases where, e.g., one bin contained most of the counts and the others had very poor counting statistics (see Sections 3.1 and 3.2.2). The fourth criterion discards sources with large off-axis angles, which have generally poorer S/Ns due to the degraded PSF, and it also guarantees each source is covered by almost all observations.

Sixty-eight sources are selected with 649–11283 counts; the median number of counts is 1399. Figure 2 shows the distribution of our counts. Our sources generally have more counts than those in previous studies, usually by substantial factors (Table 1), allowing improved source characterization. The faintest selected sources have fluxes (observed-frame 0.5–7 keV; see Section 3.2.2 for flux calculation) of $\approx 1 \times 10^{-15}$ erg cm^{-2} s^{-1}, similar to the full-band source

detection limit of the *Chandra* COSMOS-Legacy survey (e.g., Civano et al. 2016). We are thus characterizing in this work the AGNs responsible for producing much of the cosmic accretion power; our measurements probe ≈20–3 times below the knee luminosity, L_X^*, of the X-ray luminosity function at $z = 0.5$–4 (e.g., Ueda et al. 2014; Aird et al. 2015).

The spectroscopic and photometric redshift data are compiled by L16. For each source, we adopt the spectroscopic redshift (z_{spec}) either marked as "secure" by L16 or consistent with the photometric redshift (z_{phot}) measurement (i.e., z_{phot} differs from z_{spec} by less than 10%). Otherwise, if z_{spec} is not available or disagrees with z_{phot}, we adopt z_{phot} because "insecure" z_{spec} are less reliable than z_{phot}. Those insecure z_{spec} are often based on spectra with few features, e.g., a tentative single absorption line, but z_{phot} are derived from SED fitting of $\gtrsim$15 photometric bands (Luo et al. 2010; Hsu et al. 2014). In total, we have 55 z_{spec} and 13 z_{phot}. The z_{phot} quality is generally high (fractional errors ∼ a few percent) thanks to the wide multi-band photometric coverage used to derive z_{phot} (Luo et al. 2010; Hsu et al. 2014). The redshift and intrinsic X-ray luminosity L_X[15] distributions of the sample are plotted in Figure 3, with the L_X values for some representative local AGNs marked for comparison purposes. The median L_X of our sources is 4×10^{43} erg s^{-1}, several times larger than that of the whole CDF-S AGN sample ($\approx 8 \times 10^{42}$ erg s^{-1}, L16); the median redshifts of the two samples are similar (≈1.5). Many local well-known AGNs have L_X within our luminosity coverage, and thus our sources, at least in this sense, appear to be distant analogs of these local AGNs.

We classify a source as type I if any broad emission line is reported in the redshift literature (20 sources); if only narrow emission lines/absorption lines are reported (35 sources) we assign a type II classification. We caution that there might be some intrinsic type I objects misclassified as type II due to, e.g., lack of spectral coverage of the hydrogen Balmer lines (e.g., Khachikian & Weedman 1974) or the spectral S/N not being sufficient to identify broad lines. If the spectral classification of a source is not available in the literature, it is classified based on fitting of the SED (data from Hsu et al. 2014): if its rest-frame optical color is blue (i.e., rest-frame $u - g < 0.8$)[16] we classify it as type I; otherwise we classify it as type II. This color classification scheme results in four type I and nine type II AGNs in addition to the spectral classification. Therefore, our sample consists of 24 type I and 44 type II AGNs. The optical classification is broadly consistent with X-ray classification approaches (i.e., using the epoch mean $N_H = 10^{22}$ cm^{-2} as the threshold for type II; see Section 3.2.1) despite some exceptions (see Figure 8). Type I sources generally have more counts than type II sources; their median counts are 2199 and 1098, respectively. Table 3 lists the properties of individual sources in our sample.

BAL quasars often show heavy and complex X-ray absorption despite their type I nature (e.g., Gallagher et al. 2002, 2006). It is of interest to investigate their X-ray variability behavior (e.g., Gallagher et al. 2004; Saez et al. 2012). There are eight type I quasars in our sample, if we define quasars as AGNs with $L_X > 10^{44}$ erg s^{-1}.[17] One of our objects has been reported as a BAL quasar (J033209.4–274806, e.g., Szokoly et al. 2004) at $z = 2.81$; it is X-ray luminous ($L_X \approx 3 \times 10^{44}$ erg s^{-1}) and highly obscured ($N_H \approx 2 \times 10^{23}$ cm^{-1}) with an intrinsic power-law photon index $\Gamma = 1.68$ (see Section 3.2). This small number of BAL quasars is expected considering only ≈20% of type I quasars are BAL quasars (e.g., Hewett & Foltz 2003; Gibson et al. 2009).

Three of our sources, J033247.8–274232 at $z = 0.98$, J033211.3–275213 at $z = 3.74$, and J033212.9–275236 at $z = 2.56$, were potentially detected in the *NuSTAR* hard band

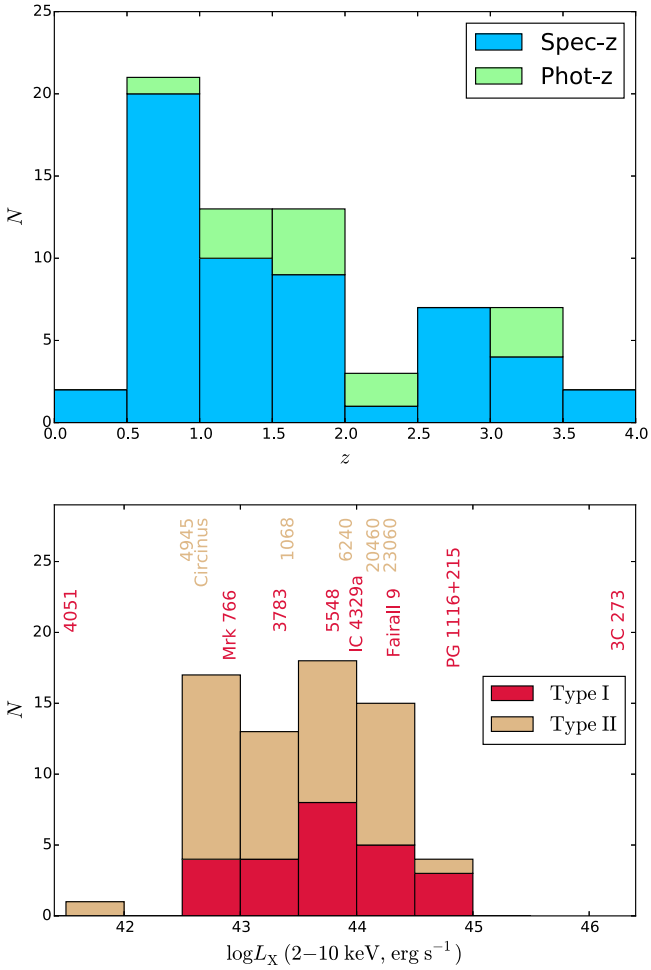

Figure 3. Upper panel: redshift histogram for our 68 sources. The blue and green bars indicate sources with spectroscopic redshifts and photometric redshifts, respectively. Lower panel: absorption-corrected X-ray luminosity (2–10 keV, rest-frame) histogram. The red and brown bars indicate type I and type II AGNs, respectively. The values are the epoch mean L_X described in Section 3.2.1. Along the top of the panel, we label the typical absorption-corrected L_X values for some representative type I (red) and type II (brown) AGNs in the local universe. The four-digit and five-digit numbers indicate NGC and IRAS sources, respectively. The L_X data were compiled from the literature (e.g., Brandt et al. 1997; Ogasaka et al. 1997; Reynolds 1997; George et al. 2000; Pounds et al. 2003; Arévalo et al. 2014; Puccetti et al. 2014, 2016; Bauer et al. 2015). Our sources cover wide ranges of both z and L_X. In terms of L_X, our sources appear to be distant analogs of many local Seyfert galaxies and moderate-luminosity quasars.

[15] Absorption-corrected X-ray luminosity in the rest-frame 2–10 keV band; we use the epoch mean value (see Section 3.2.1).

[16] This threshold generally separates our type I and type II AGNs classified by spectral features; see, e.g., Richards et al. (2002) and Barger et al. (2003) for the effectiveness of optical color classifications.

[17] Corresponding to $L_\nu(2500\ \text{Å}) \sim 10^{30}$ erg s^{-1} Hz^{-1} calculated from the α_{OX}-L_ν(2500 Å) relation presented in Just et al. (2007).

Table 3
Source Properties

Name (CXOCDFS) (1)	R.A. (2)	Decl. (3)	z (4)	Δz (5)	Opt. Type (6)	Off-axis (7)	Counts (8)	$P_{\rm PF}$ (9)	$P_{\rm HR}$ (10)	$E_{\rm peg}$ (11)	*goodness* (12)	Γ (13)
J033158.1–274833	52.99210	−27.80943	0.74	n/a	IIs	6.69	1366.0	0.00	32.75	0.50	10.2	1.52
J033158.2–275041	52.99283	−27.84490	3.31	0.09	Ic	7.05	2684.8	0.00	86.68	0.96	0.5	1.72
J033200.3–274319	53.00150	−27.72209	1.04	n/a	Is	7.96	3598.1	0.00	60.04	0.50	1.0	1.78
J033201.5–274327	53.00663	−27.72420	2.73	n/a	Is	7.67	2772.0	0.00	15.30	0.66	4.8	1.72
J033202.4–274600	53.01026	−27.76675	1.62	n/a	Is	6.18	2012.5	0.00	61.65	0.50	7.3	1.65

Note. The full table contains 21 columns of information for 68 sources. Column (1): standard name of *Chandra* CDF-S sources. Columns (2) and (3): J2000 coordinates. Column (4): adopted redshift.; see L16 for redshift references. Column (5): 1σ errors of photometric redshift. n/a indicates a spectroscopic redshift has been used. Column (6): optical spectral type (see Section 2.2 for the classification scheme). Is (IIs): type I (II) from spectral classification; Ic (IIc): type I (II) from color classification. The spectral classifications are from Szokoly et al. (2004), Mignoli et al. (2005), Ravikumar et al. (2007), Tozzi et al. (2009), Treister et al. (2009), Silverman et al. (2010), and Mao et al. (2012). Column (7): off-axis angle in units of arcminutes. Column (8): full-band (0.5–7 keV) total available net counts (not aperture corrected). Columns (9) and (10): p-value of photon flux and hardness ratio variability, respectively (Section 3.1). Both are in units of %. Column (11): the lower end of the normalization band used in *pegpwrlw*, in units of keV (Appendix A). Column (12): *goodness* of the spectral fitting (*wabs* × *zwabs* × *pegpwrlw* model), in units of % (Section 3.2.1). Column (13): power-law photon index. Columns (14) and (15): epoch mean values of intrinsic $L_{\rm X}$ (rest-frame 2–10 keV, in units of erg s^{-1}) and $N_{\rm H}$ (in units of cm^{-2}), respectively (Section 3.2.1). Columns (16) and (17): metrics ($\Delta{\rm AIC}_L$ and $\Delta{\rm AIC}_N$) of the significance of $L_{\rm X}$ and $N_{\rm H}$ variability, respectively (Section 3.2.3). Columns (18) and (19): normalized excess variance of $L_{\rm X}$ variability ($\sigma^2_{{\rm exc},L}$) and its uncertainty, respectively (Section 3.2.5). Columns (20) and (21): normalized excess variance of $N_{\rm H}$ variability ($\sigma^2_{{\rm exc},N}$) and its uncertainty, respectively (Section 3.2.5). We only calculated this quantity for the 35 sources with all four epochs having $\delta N_{{\rm H},i}/N_{{\rm H},i} < 0.4$ (see Appendix A); n/a indicates the other 33 sources.

(This table is available in its entirety in machine-readable form.)

(8–24 keV; Mullaney et al. 2015). The matching between *Chandra* and *NuSTAR* sources was performed by Mullaney et al. (2015). J033247.8–274232 has an almost unambiguous *NuSTAR* counterpart because it is the only bright *Chandra* source within 23″ (≈3 times the typical *NuSTAR* positional uncertainty) of the *NuSTAR* source position. J033211.3–275213 and J033212.9–275236 are matched to a single *NuSTAR* source and are both ≈15″ from the *NuSTAR* counterpart. There are no other bright *Chandra* sources within 23″ of this *NuSTAR* source position. Therefore, one of these two high-redshift *Chandra* sources likely has a *NuSTAR* hard-band detection.

3. DATA ANALYSES

3.1. Photometric Variability

3.1.1. Method

We use full-band (0.5–7 keV) photometry to analyze photon flux (PF, i.e., count rate per unit area, in units of counts s^{-1} cm^{-2}) variability. For each epoch of a source, we calculate PF as

$$\mathrm{PF}_i = \frac{net\_counts_i}{effarea_i \times exptime_i}, \quad (1)$$

and its uncertainty

$$\delta\mathrm{PF}_i = \frac{\delta net\_counts_i}{effarea_i \times exptime_i}, \quad (2)$$

where the subscript i denotes the epoch; net_counts_i and δnet_counts_i[18] are background-subtracted counts and the corresponding error, respectively; $effarea_i$ and $exptime_i$ are the effective area and exposure time, respectively. The effective area is approximated as the average ancillary response file (ARF) weighted by the average CDF-S AGN spectrum (i.e., a $\Gamma = 1.4$ power law with Galactic absorption; see, e.g., Paolillo et al. 2004). This procedure accounts for the varying sensitivity of *Chandra* among different epochs due to, e.g., quantum-efficiency degradation and gaps between CCDs since these factors are considered by AE when calculating the ARF. Figure 4 shows light curves of the six sources with the most counts.

To identify variable sources, we calculate the statistic

$$X^2_{\rm PF} = \sum_{i=1}^{4} \frac{(\mathrm{PF}_i - \langle \mathrm{PF} \rangle)^2}{(\delta \mathrm{PF}_i)^2}, \quad (3)$$

where $\langle \mathrm{PF} \rangle$ is the unweighted mean of PF_i (e.g., Turner et al. 1999).[19] For sources with large numbers of counts, the probability distribution of PF approaches the normal distribution, and thus $X^2_{\rm PF}$ should follow the χ^2 distribution with three degrees of freedom ($\chi^2_{\rm dof=3}$). Our sources have at least 600 total net counts (at least ∼150 counts or S/N ∼ 12 per bin). Therefore $\chi^2_{\rm dof=3}$ should be a good approximation of $X^2_{\rm PF}$. To verify this point and find an accurate p-value ($P_{\rm PF}$) from $X^2_{\rm PF}$, we adopt a Monte Carlo simulation strategy similar to that in Paolillo et al. (2004) and Young et al. (2012). The null hypothesis is that PF remains constant in the four epochs at $\mathrm{PF}_{\rm mean}$. To perform the simulations, we need to know model counts in each epoch. We convert $\mathrm{PF}_{\rm mean}$ to the net counts expected in each epoch as

$$net\_counts_i^{\rm model} = \mathrm{PF}_{\rm mean} \times effarea_i \times exptime_i. \quad (4)$$

[18] We use the average of upper and lower 1σ errors here, which are calculated by AE using Gehrels (1986).

[19] We have tested using the mean weighted by $1/(\delta\mathrm{PF}_i)^2$, and obtained similar results. This is also true for the hardness ratio variability.

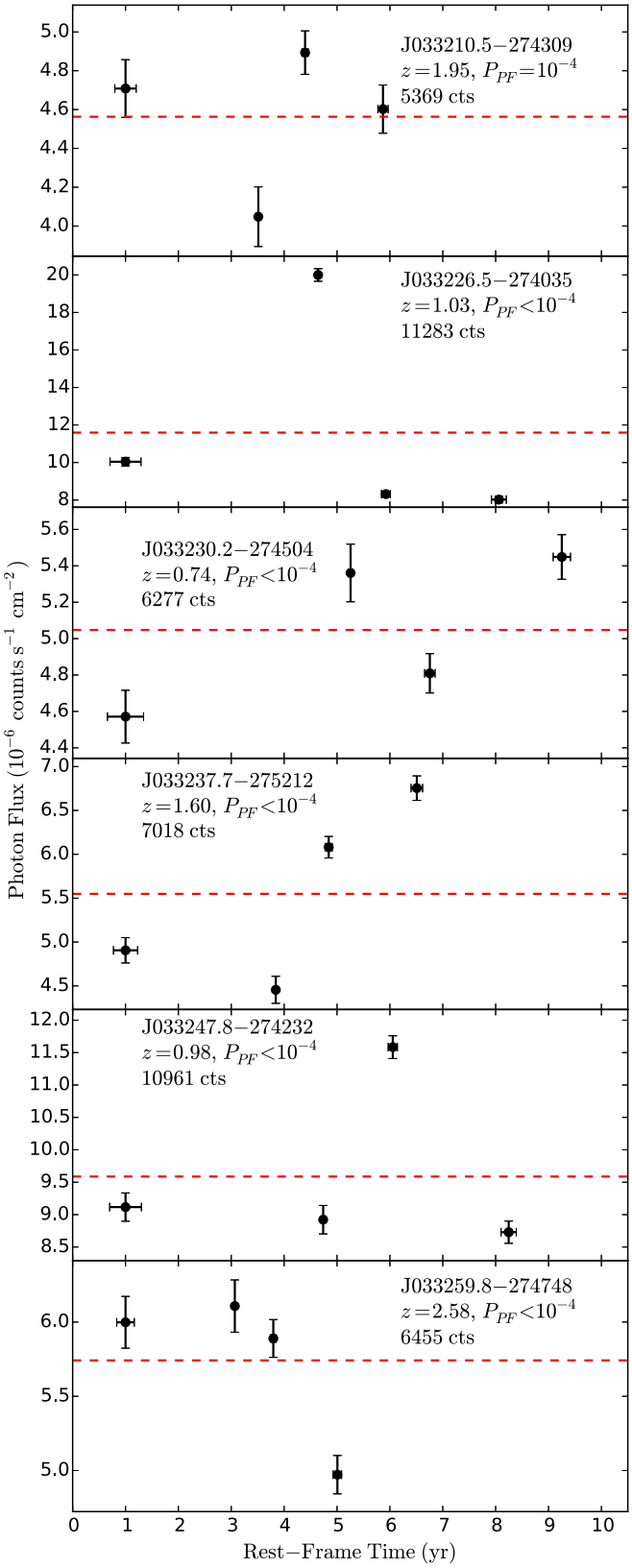

Figure 4. Light curves of the six sources with the most counts. The red dashed horizontal lines indicate the unweighted mean of photon fluxes for each source. The horizontal error bars indicate the bin width of each epoch. The rest-frame time of epoch 1 is set to 1 year. Some source properties are labeled on the corresponding panels. All of the six sources show photon flux variability (i.e., $P_{\rm PF} < 5\%$).

We obtain the model source counts (not background subtracted) and model background counts as

$$src\_counts_i^{\rm model} = net\_counts_i^{\rm model} + \frac{bkg\_counts_i^{\rm observed}}{backscal_i},$$
$$bkg\_counts_i^{\rm model} = bkg\_counts_i^{\rm observed}, \quad (5)$$

where *backscal* is the factor produced by AE that scales background counts (usually obtained in a large aperture) to the source-extraction aperture. We use $src\_counts_i^{\rm model}$ ($bkg\_counts_i^{\rm model}$) as the mean in a Poisson distribution to simulate src_counts_i (bkg_counts_i) and extract photometry following the algorithm in AE.[20] We obtain the $X^2_{\rm PF}$ for a simulated data set (10,000 simulations) following the same procedures as described above. We perform Kolmogorov–Smirnov (KS) tests between the simulated $X^2_{\rm PF}$ distributions and the $\chi^2_{\rm dof=3}$ distribution. The resulting KS statistics for our sources have a median 0.015; this small value indicates our simulated $X^2_{\rm PF}$ distributions are very similar to the $\chi^2_{\rm dof=3}$ distribution.

We define the hardness ratio (HR) for a source in an epoch as

$$\mathrm{HR}_i = \frac{\mathrm{PF}_{i,\rm hard} - \mathrm{PF}_{i,\rm soft}}{\mathrm{PF}_{i,\rm hard} + \mathrm{PF}_{i,\rm soft}}, \quad (6)$$

where $\mathrm{PF}_{i,\rm hard}$ and $\mathrm{PF}_{i,\rm soft}$ are PFs as defined above but for the hard band (2–7 keV) and soft band (0.5–2 keV), respectively. We estimate the error of HR from error propagation as

$$\delta\mathrm{HR}_i = \frac{2\mathrm{PF}_{i,\rm hard}\mathrm{PF}_{i,\rm soft}}{(\mathrm{PF}_{i,\rm hard} + \mathrm{PF}_{i,\rm soft})^2} \times \sqrt{\left(\frac{\delta\mathrm{PF}_{i,\rm hard}}{\mathrm{PF}_{i,\rm hard}}\right)^2 + \left(\frac{\delta\mathrm{PF}_{i,\rm soft}}{\mathrm{PF}_{i,\rm soft}}\right)^2}. \quad (7)$$

To identify HR-variable sources, we calculate

$$X^2_{\rm HR} = \sum_{i=1}^{4} \frac{(\mathrm{HR}_i - \langle \mathrm{HR} \rangle)^2}{(\delta \mathrm{HR}_i)^2}, \quad (8)$$

where $\langle \mathrm{HR} \rangle$ is the unweighted mean of HR_i.

We perform simulations similar to those above to convert $X^2_{\rm HR}$ to a *p*-value ($P_{\rm HR}$). The null hypothesis is that HR_i is constant and equals $\mathrm{HR}_{\rm mean}$ over the four epochs. We approximate the model full-band net counts as the sum of the observed hard-band and soft-band net counts,

$$net\_counts_{i,\rm full}^{\rm model} = net\_counts_{i,\rm hard}^{\rm observed} + net\_counts_{i,\rm soft}^{\rm observed}. \quad (9)$$

[20] See Section 5.10 of the AE manual available at http://www2.astro.psu.edu/xray/docs/TARA/ae_users_guide.html.

The model hard-band and soft-band net counts are calculated by

$$\begin{aligned} & net\_counts_{i,\mathrm{hard}}^{\mathrm{model}} \\ & \quad = net\_counts_{i,\mathrm{full}}^{\mathrm{model}} \\ & \qquad \times \left(\frac{net\_counts_{i,\mathrm{hard}}}{net\_counts_{i,\mathrm{hard}} + net\_counts_{i,\mathrm{soft}}} \right)^{\mathrm{model}} \\ & \quad = net\_counts_{i,\mathrm{full}}^{\mathrm{model}} \\ & \qquad \times \frac{1}{2} \left(1 + \left(\frac{net\_counts_{i,\mathrm{hard}} - net\_counts_{i,\mathrm{hard}}}{net\_counts_{i,\mathrm{hard}} + net\_counts_{i,\mathrm{soft}}} \right)^{\mathrm{model}} \right) \\ & \quad = net\_counts_{i,\mathrm{full}}^{\mathrm{model}} \times \frac{1 + \mathrm{HR}_{\mathrm{mean}}}{2} \end{aligned} \tag{10}$$

and

$$\begin{aligned} & net\_counts_{i,\mathrm{soft}}^{\mathrm{model}} \\ & \quad = net\_counts_{i,\mathrm{full}}^{\mathrm{model}} - net\_counts_{i,\mathrm{hard}}^{\mathrm{model}}, \end{aligned} \tag{11}$$

respectively.

Knowing $net\_counts_{i,\mathrm{hard(soft)}}^{\mathrm{model}}$, we obtain $src\_counts_{i,\mathrm{hard(soft)}}^{\mathrm{model}}$ and $bkg\_counts_{i,\mathrm{hard(soft)}}^{\mathrm{model}}$ using Equation (5). Similar to the case of X_{PF}^2, the simulated X_{HR}^2 distributions are close to the $\chi_{\mathrm{dof}=3}^2$ distribution. The KS statistics derived from comparing simulated X_{HR}^2 distributions and $\chi_{\mathrm{dof}=3}^2$ have median 0.023.

3.1.2. Results

The histograms of P_{PF} and P_{HR} are presented in Figure 5. Using $P = 5\%$ as the threshold for variability ($\sim 68 \times 5\% \lesssim 4$ false positives expected), 90% (61/68) and 16% (11/68) of our sources display PF variability and HR variability, respectively. All of our six sources with the most counts are variable (see Figure 4). Changing the threshold to $P = 1\%$ ($\sim 68 \times 1\% \lesssim 1$ false positive expected) leads to a PF-variable fraction and an HR-variable fraction of 84% (57/68) and 9% (6/68), respectively. This PF-variable fraction (84%) is higher than that of optically selected Sloan Digital Sky Survey (SDSS, York et al. 2000) quasars under the same confidence level (i.e., 65%; the sample is from G12 with the same count constraint of 600 applied). This result supports an intrinsic anticorrelation between variability amplitude and X-ray luminosity (see Section 3.2.6), considering those SDSS quasars are generally $\approx$10 times more X-ray luminous than our sources (see Table 1 and Section 3.2.3). However, this behavior might also be a result of different rest-frame time samplings (see Figure 1). With the $P = 5\%$ threshold, almost all (23/24) type I AGNs and 86% (38/44) of type II AGNs are PF variable; 13% (3/24) of type I AGNs and 18% (8/44) of type II AGNs are HR variable. The higher PF variable source fraction for type I sources might be due to their higher numbers of counts (Figure 2). Type II sources are more likely to be HR variable despite their smaller numbers of counts. However, Fisher's exact test shows that the dependences of variable source fractions on optical spectral type are not statistically significant.

3.1.3. Variability within Each Epoch

We also use each *Chandra* observation as a bin to analyze the variability within each epoch ($\lesssim$1 year, observed-frame).

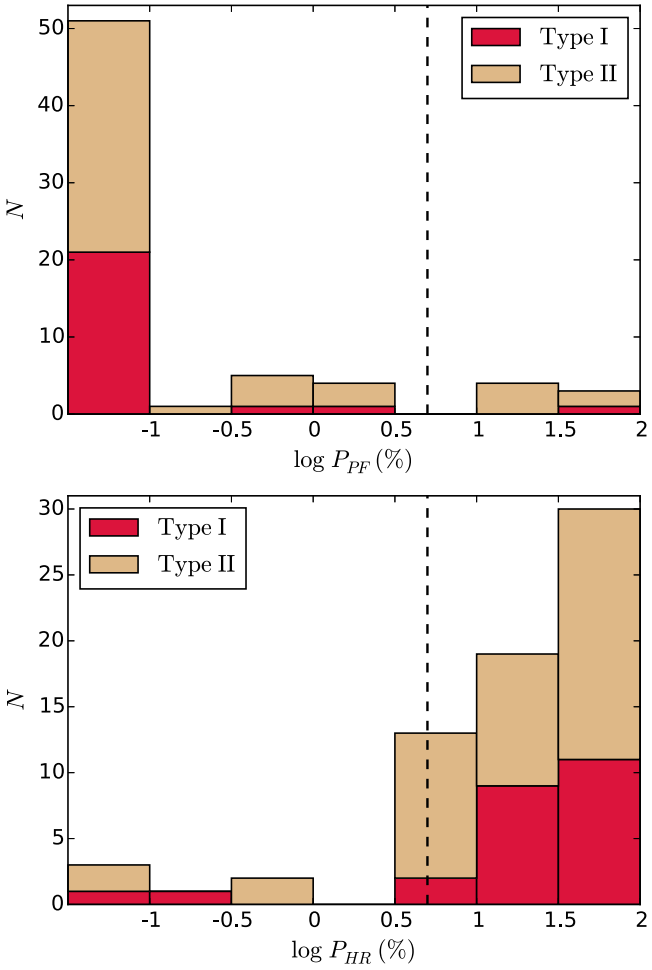

Figure 5. Histograms of P_{PF} (upper panel) and P_{HR} (lower panel). The red and brown bars indicate type I and type II AGNs, respectively. The vertical black dashed lines in both panels indicate the value of 5%, our variability criterion. The leftmost column indicates all sources with P_{PF} (P_{HR}) $< 0.1\%$. Photon flux variability is generally more common than hardness ratio variability.

The observation lengths range from about 30 to 100 ks (see L16). We calculate P_{PF} and P_{HR} for each source within each of the four epochs. The method is the same as described in Section 3.1.1. PF variability is still significant: the PF variable (i.e., $P_{\mathrm{PF}} < 5\%$) source fractions are 49%, 29%, 56%, and 38% for each bin, respectively.[21] We find the variable source fraction is higher for sources with more counts, likely due to their higher S/N. We do not detect statistically significant HR variability: the HR-variable (i.e., $P_{\mathrm{HR}} < 5\%$) source fractions are 3%, 3%, 1%, and 3%, respectively, consistent with the expected false positive rate. This result is likely due to the low S/N in this data set compared to that of the binned data.

More detailed analyses based on such a binning strategy will be presented in another paper (X. C. Zheng et al., in preparation). Those analyses suggest that short-term (days-to-months) variability of our sources by large amplitudes (e.g., more than a factor of two) is rare, similar to our results on long timescales (Sections 3.2.2 and 3.2.5).

[21] Besides random fluctuations, there are many factors, including total exposure time and epoch bin width, that can affect the detected variable source fraction for each epoch.

3.2. Spectral Variability

3.2.1. Method

The photometric analyses in Section 3.1 roughly evaluate the spectral normalization and shape changes. To characterize the spectral variability more accurately as well as gain improved physical insights, we perform spectral fitting for each source. The fitting is based on full-band (observed-frame 0.5–7 keV) spectra to maximize the available counts. Given our high-quality X-ray spectra (with a median full-band S/N ≈ 17 in each epoch) owing to the good angular resolution and low source-cell background of *Chandra*, we can still do reliable spectral fitting even though the counts per epoch (median ~350) are moderate. Note that we are typically accessing penetrating rest-frame X-rays up to ≈10–30 keV.

We use XSPEC v12.9.0i (Arnaud 1996) to carry out spectral fitting. Counts are not binned over different ACIS pulse height amplitude (PHA) channels, and the Cash statistic (Cash 1979) is used for fitting. Considering the available counts, we adopt a simple fitting model of a power law with Galactic and intrinsic absorption *wabs* × *zwabs* × *pegpwrlw* (see Morrison & McCammon 1983 for the *wabs* and *zwabs* models). We adopt *pegpwrlw* (normalized over a finite energy band) instead of the widely used *powerlaw* (normalized at observed-frame 1 keV) for the reasons described in Appendix A. We fix the redshift (*zwabs*) as the adopted value in Section 2.2. The allowed ranges of $N_{\rm H}$ (*zwabs*) and Γ (*pegpwrlw*) are set to 10^{19}–10^{24} $\rm cm^{-2}$ and 1.2–2.4, respectively. The counts of our sources in each epoch (median ~350) generally cannot constrain Γ effectively; e.g., Brightman et al. (2013) found that even a simple *powerlaw* model would require $\gtrsim$1000 counts to obtain an uncertainty (90% confidence level) of Γ within 0.2. Studies of quasars and local luminous AGNs show that spectral variability generally follows a "softer when brighter" behavior (e.g., Sobolewska & Papadakis 2009; Gibson & Brandt 2012; Sarma et al. 2015; Connolly et al. 2016).[22] However, based on the empirical X-ray flux–Γ relations given by those studies, the Γ variability amplitudes for our sources are expected to be small and not detectable given the counts we have in each epoch. For example, flux variability by a factor of two (about the upper limit of our flux variability amplitudes; see Section 3.2.2) only produces $\Delta\Gamma \approx 0.1$. Motivated by this expected near constancy of Γ, we thus simultaneously fit the spectra of all four epochs by linking their photon indices Γ (*pegpwrlw*), assuming no substantial Γ variability. Considering the low source-cell backgrounds and high count numbers for our sources, we do not specifically model the background but employ the XSPEC default background modeling strategy.[23] The $norm_i$ (i.e., normalization of *pegpwrlw*) and $N_{{\rm H},i}$ (*zwabs*) are set free and not linked across epochs, where subscripts i denote the epoch indices. This spectral fitting yields best-fit model parameters, i.e., $\Gamma_{\rm fit}$, $norm_i$, and $N_{{\rm H},i}$, and the errors of $norm_i$. The errors of $N_{{\rm H},i}$ are estimated with the method detailed in Appendix A. This method is critical for obtaining accurate errors of $N_{{\rm H},i}$ for the reasons explained in Appendix A. The $\Gamma_{\rm fit}$ distribution is shown in Figure 6. The distribution is similar to that found by Tozzi et al. (2006), except that our dispersion is smaller likely due to our larger numbers of counts. We set both Galactic and intrinsic absorption to none and calculate the absorption-corrected X-ray luminosity in the rest-frame 2–10 keV band for each epoch. The unweighted mean luminosity (absorption column density) of the four epochs is denoted as $L_{\rm X}$ ($N_{\rm H}$) and widely used throughout this paper.

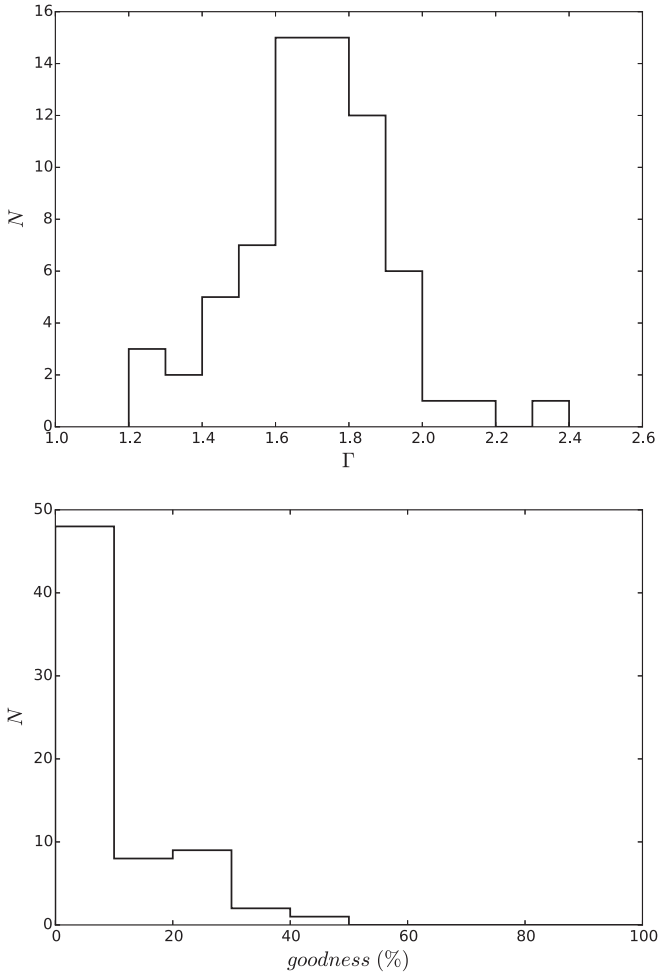

Figure 6. Upper panel: best-fit Γ histogram. Lower panel: *goodness* histogram. The *goodness* distribution indicates the *wabs* × *zwabs* × *pegpwrlw* model generally describes our data acceptably.

Since we fit the unbinned spectra with the Cash statistic, the spectral-fit quality cannot be inferred directly from the best-fit statistic, e.g., χ^2/dof in the minimum χ^2 fitting case. Instead, we perform goodness-of-fit Monte Carlo simulations for each source in XSPEC.[24] XSPEC simulates 1000 spectra from the best-fit parameters and calculates the fraction (*goodness*) of simulated spectra with a KS statistic less than that of the observed spectrum. Here, the KS statistic is used to describe the "similarity" between a spectrum and the model, similar to χ^2 in the minimum χ^2 fitting case. In other words, *goodness* can be interpreted as the confidence level of rejecting the model. The distribution of *goodness* is presented in Figure 6. The fits are acceptable (*goodness* < 50%, e.g., Corral et al. 2015) for all our sources. The worst case is J033218.3–275055 with

[22] This behavior likely changes when the Eddington ratio is low (i.e., $\lesssim 10^{-3}$; e.g., Yang et al. 2015; Connolly et al. 2016), but the Eddington ratios for our sources are likely to be higher than this threshold, considering their luminosities (see Figure 3) and that they are the X-ray brightest AGNs in the CDF-S.

[23] See https://heasarc.gsfc.nasa.gov/xanadu/xspec for details.

[24] For more details, see https://heasarc.gsfc.nasa.gov/xanadu/xspec/manual/XSappendixStatistics.html and http://xraygroup.astro.noa.gr/Webpage-prodec/documentation.html#good.

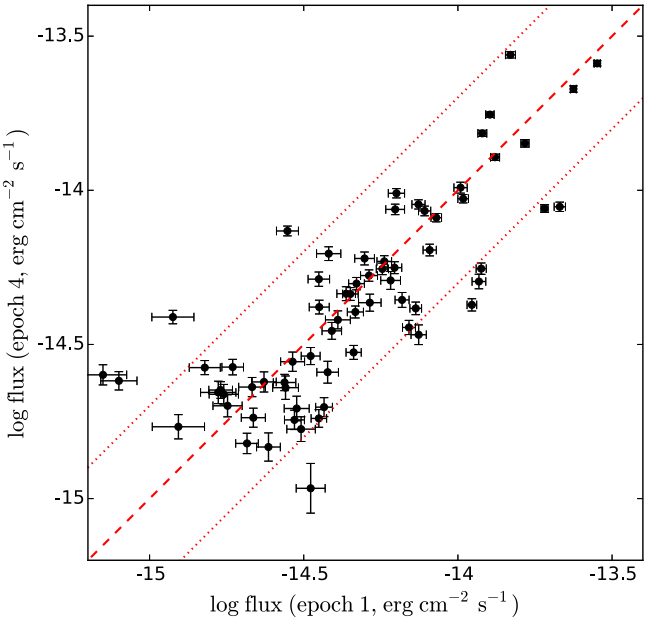

Figure 7. Flux (epoch 4) vs. flux (epoch 1). The fluxes are calculated from our spectral fitting results (see Section 3.2.1), and are not corrected for Galactic or intrinsic absorption. The energy band is observed-frame 0.5–7 keV (i.e., full-band). The red dashed line indicates no flux change; the red dotted lines indicate flux changes by a factor of two. The ranks of fluxes are similar in the two epochs. Thus, X-ray variability over 15 years does not significantly affect the appearance of the overall X-ray source population.

goodness = 44%, a Compton-thick candidate reported in the literature (Tozzi et al. 2006; Comastri et al. 2011). A detailed discussion of this source is presented in Appendix B.

3.2.2. Flux Variability over 15 Years

Long-term X-ray variability may affect physical inferences about X-ray source populations, e.g., the star formation versus AGN activity connection may be affected by ∼Myr timescale AGN variability (e.g., Hickox et al. 2014). It is thus of interest to assess whether X-ray variability on the longest observable timescales (i.e., between epoch 1 and epoch 4) substantially affects the appearance of the overall X-ray source population.

Figure 7 displays the full-band fluxes of epoch 1 and epoch 4. Applying Spearman's test on the fluxes of epoch 1 and epoch 4 yields $\rho = 0.82$ and a p-value of 10^{-17}; the large value of ρ indicates a good association of ranks. In general, the brightest (faintest) sources remain the brightest (faintest) after 15 years. Only 11 ($11/68 = 16\%$) sources have flux changes greater than a factor of two. Qualitatively similar results are obtained when we pair any two of our available epochs.

The rarity of extremely variable sources in the distant universe over long timescales is broadly consistent with a recent study focusing on low-redshift AGNs (Strotjohann et al. 2016). Our results prove that, at least on a 15 year observed-frame timescale, basic inferences about distant AGN source populations are not strongly affected by variability, e.g., the expected star formation versus AGN activity connection is unlikely to be hidden by AGN variability on a rest-frame timescale of ∼5–10 years. These results also show that X-ray changing-look AGNs are rare, and they constrain the frequency of other types of novel long-term X-ray variability (see Section 1). Setting direct X-ray constraints on much longer timescales is unfortunately limited by, e.g., the age of X-ray astronomy. Cosmic X-ray surveys often bin observations performed over 1–15 years; our results indicate that long-term variability is not likely to affect greatly the interpretation of such survey results.

3.2.3. Identification of L_X- and N_H-Variable Sources

We identify L_X- and N_H-variable sources using the Akaike information criterion (AIC, Akaike 1974). The AIC is based on information theory and does not assume a particular model-fitting technique or distribution of uncertainties (e.g., Burnham & Anderson 2002; Kelly et al. 2007; Buchner et al. 2014). AIC is defined as $\mathrm{AIC} = C + 2k$, where C is the fitting statistic (i.e., the Cash statistic in our case) and k is the number of free parameters in the model.[25] Models with smaller AIC are considered to be more probable.

For each source, we calculate AIC (denoted as AIC_0) for the spectral fitting results in Section 3.2.1. To evaluate the significance of L_X variability, we link $norm_i$ in all spectra of the four epochs[26] and redo the fitting. Other settings of the model are the same as in Section 3.2.1. We calculate AIC for the new fitting results, denoted as AIC_1. We use the difference $\Delta\mathrm{AIC}_L = \mathrm{AIC}_1 - \mathrm{AIC}_0$ to evaluate the significance of L_X variability. If $\Delta\mathrm{AIC}_L > 4$ (e.g., Burnham & Anderson 2002),[27] we assign this source as an L_X-variable source. Similarly, we identify N_H-variable sources by calculating the AIC difference $\Delta\mathrm{AIC}_N$ between N_H-linked and unlinked models and comparing it with the threshold of four. The $\Delta\mathrm{AIC}_L$ and $\Delta\mathrm{AIC}_N$ for each source are listed in Table 3.

The resulting L_X- and N_H-variable source fractions are 74% (50/68) and 16% (11/68), respectively. Four of the 11 N_H-variable sources are HR-variable (Section 3.1).[28] The other seven sources have large P_{HR} values (>10%). One reason for this result is likely to be that the definition of HR (Equation (6)) uses observed-frame 2 keV as the boundary between the soft and hard bands. This choice of 2 keV is just by convention. It corresponds to different rest-frame energies for different sources and might not be sensitive in selecting some N_H-variable sources. We checked the four-epoch spectra of the seven sources, and found that 2 keV as a boundary is either too high or too low to detect their N_H variability effectively.

Most (10/11) N_H variable sources are also L_X variable. The median $\Delta\mathrm{AIC}_L$ ($\Delta\mathrm{AIC}_N$) for L_X-variable (N_H-variable) sources is 43 (6.2). Therefore, our L_X variability is generally more significant than N_H variability. The BAL quasar J033209.4–274806 shows L_X variability ($\Delta\mathrm{AIC}_L = 4.9$) but not N_H variability ($\Delta\mathrm{AIC}_N = -2.7$). We investigate three significantly variable sources, J033226.5–274035, J033259.7–274626, and J033229.9–274530, as illustrative examples in Appendix C. Notably, J033229.9–274530

[25] Note that we do not need to use the AICc, the corrected AIC designed for the cases where sample size n is $\approx k^2$. This is because our n = number of spectral PHA bins for all four epochs together (≈2000) is much greater than k^2 (≈50).

[26] Hereafter, we use the parameter *norm* to evaluate L_X variability, since L_X is proportional to *norm* for a given source assuming no Γ variability.

[27] We have also performed classic χ^2 tests for variable source identification, assuming our errors are Gaussian. For both L_X and N_H variability, we find good correlations between ΔAIC and $\chi^2_{\mathrm{dof}=3}$, with $\Delta\mathrm{AIC} = 4$ corresponding to $\chi^2_{\mathrm{dof}=3} \approx 10$ (i.e., p-value ≈ 2%). However, we prefer the AIC approach because it does not rely on the assumption of Gaussian errors.

[28] Our AIC method selects variable sources at a significance level of ≈98% (see Footnote 27). Only six sources show HR variability at this significance level (i.e., $P_{HR} < 2\%$), and all four N_H-variable and HR-variable sources are included among these six.

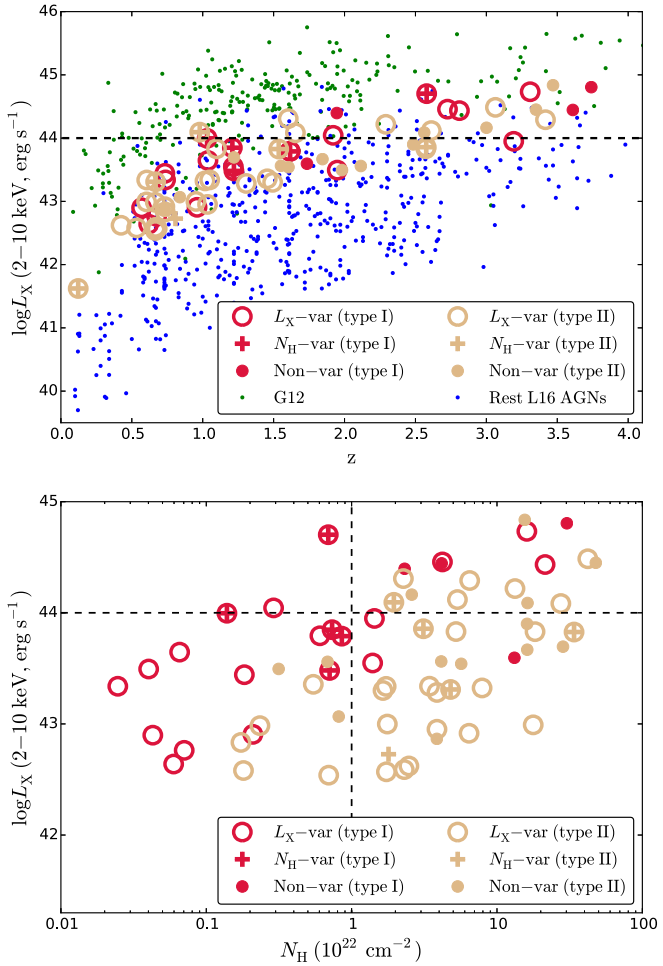

Figure 8. Upper panel: L_X vs. z. The open circles, crosses, and solid circles indicate L_X-variable, N_H-variable, and non-variable sources, respectively. A source can be both L_X-variable and N_H-variable. Red and brown colors indicate type I and type II sources, respectively. The green and the blue points indicate G12 quasars and the rest of the AGNs in L16. At a given redshift, our sources are generally less luminous than G12 quasars and more luminous than the other L16 AGNs. The dashed horizontal line indicates our definition of quasars (i.e., $L_X > 10^{44}$ erg s^{-1}, see Section 2.2). Lower panel: L_X vs. N_H. The symbols have the same meanings as for the upper panel. The horizontal and vertical dashed lines indicate our definition of quasars and the common definition of X-ray obscured AGNs (i.e., $N_H > 10^{22}$ cm^{-2}), respectively.

transitions from an X-ray unobscured to obscured state. The positions of the identified variable sources in the L_X–z and L_X–N_H planes are indicated in Figure 8. G12 performed similar variability analyses but for optically selected SDSS quasars. Their quasars are included in the L_X–z plot to demonstrate the differences between their sample and ours. Luminosities for the G12 objects are estimated assuming a power law with $\Gamma = 1.8$. The typical luminosity of our sources is generally about one order of magnitude lower than that of the SDSS quasars at a given redshift. The majority (≈60%) of the X-ray obscured quasars (i.e., $N_H > 10^{22}$ cm^{-2} and $L_X > 10^{44}$ erg s^{-1}) in our sample are L_X-variable, supporting the idea that we are observing their central X-ray-emitting regions directly. Also, 7 of our 11 optically classified type II quasars show L_X variability (Figure 8). The well-studied optically classified type II quasar at $z = 3.70$ in the CDF-S (e.g., Norman et al. 2002; Comastri et al. 2011) is not included in our sample due to its limited number of available counts (see Section 2.2).

3.2.4. Relation Between L_X and N_H Variability

If the observed N_H variability were caused by changes of the ionization parameter of the obscuring matter, an anticorrelation between L_X and N_H variability might be expected; when L_X rises, the obscuring matter would become more ionized and generally less opaque. We performed a Spearman's test on $L_{X,i}/L_X$ and $N_{H,i}/N_H$ for the 10 sources together that show both L_X and N_H variability, but did not find a significant anticorrelation. There is also no significant anticorrelation produced if we expand the Spearman's test to all sources. Therefore, the N_H variability is not likely to be primarily driven by changes of ionization parameter. Nevertheless, some ionization-driven N_H variability might still exist if there are year-scale time delays between L_X and N_H variability due to, e.g., a low density of the absorber (e.g., Krolik & Kriss 1995; Collinge et al. 2001).

3.2.5. Variability Amplitude Estimation

In this section, we illustrate and evaluate our method to quantify variability amplitude, and the results are used in all subsequent material. We use the normalized excess variance ($\sigma^2_{\rm exc}$, e.g., Turner et al. 1999; Vaughan et al. 2003) to estimate the intrinsic variability scale for L_X (N_H) of each source. $\sigma^2_{\rm exc}$ is calculated as

$$\sigma^2_{\rm exc} = \frac{1}{N\langle x\rangle^2}\sum_{i=1}^{N}[(x_i - \langle x\rangle)^2 - (\delta x_i)^2], \quad (12)$$

where N is the number of epochs (i.e., 4); x_i and δx_i are the best-fit $norm_i$ ($N_{H,i}$) and its 1σ error $\delta norm_i$ ($\delta N_{H,i}$), respectively; and $\langle x\rangle$ is the unweighted mean of $norm_i$ ($N_{H,i}$). The error of $\sigma^2_{\rm exc}$ is estimated as $s_D/(\langle x\rangle^2\sqrt{N})$, where

$$s_D^2 = \frac{1}{N-1}\sum_{i=1}^{N}[(x_i - \langle x\rangle)^2 - (\delta x_i)^2 - \sigma^2_{\rm exc}\langle x\rangle^2]^2. \quad (13)$$

is the variance of the summed terms $(x_i - \langle x\rangle)^2 - (\delta x_i)^2$ in Equation (12). We calculate the L_X $\sigma^2_{\rm exc}$ ($\sigma^2_{{\rm exc},L}$) for each source. We only derive the N_H $\sigma^2_{\rm exc}$ ($\sigma^2_{{\rm exc},N}$) for the 35 sources with all four epochs having $N_{H,i}$ fractional errors $\delta N_{H,i}/N_{H,i} < 0.4$ (Appendix A).

The results are listed in Table 3. While $\sigma^2_{{\rm exc},L}$ and $\sigma^2_{{\rm exc},N}$ are designed to measure intrinsic variability under ideal conditions, they may also be affected by the available counts (e.g., Allevato et al. 2013). However, the biases are minimized for high S/N, as is the case for our data (Section 3.2.1). Indeed, Spearman's test demonstrates no significant dependence of $\sigma^2_{{\rm exc},L}$ and $\sigma^2_{{\rm exc},N}$ on the number of counts.

3.2.6. Variability Dependence on Luminosity, X-ray Absorption, and Redshift

It has been well established that the strength of AGN X-ray flux variability decreases as luminosity increases on timescales from minutes to about a year (e.g., Paolillo et al. 2004; Ponti et al. 2012). Also, studies of local Seyfert galaxies show that more obscured sources tend to be less variable on short timescales (minutes to hours; e.g., Turner et al. 1997; Hernández-García et al. 2015). Therefore, it is of interest to investigate the dependence of long-term (years) variability on luminosity and absorption level. Figure 9 shows the dependence of $\sigma^2_{{\rm exc},L}$ on L_X. The unweighted mean of $\sigma^2_{{\rm exc},L}$ decreases toward higher

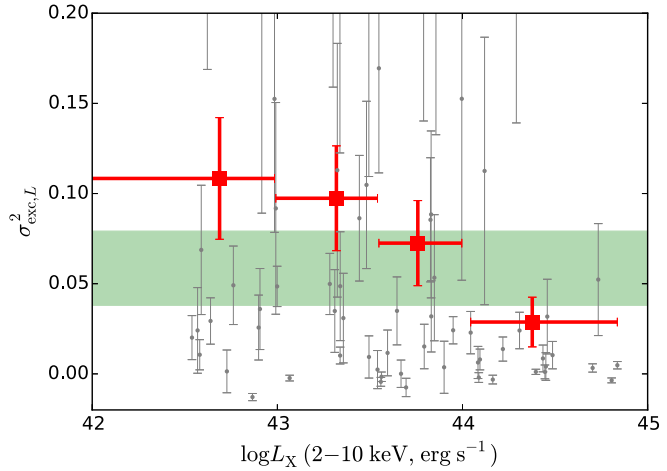

Figure 9. $\sigma^2_{\rm exc,L}$ vs. $L_{\rm X}$. $L_{\rm X}$ values are the mean values in Section 3.2.1. Gray points indicate each individual source. The red squares indicate the mean value of each bin. The red horizontal error bars indicate the bin widths; the red vertical error bars indicate the errors on the mean values calculated analytically (see Section 3.2.6). The green shaded region indicates the $\sigma^2_{\rm exc,L}$ expected from a power-law PSD with a slope of −1 (see Section 4.2). Our $\sigma^2_{\rm exc,L}$ decreases at high luminosity. This is likely caused by the fact that our highest sampling frequency exceeds the PSD break frequency of the luminous sources (Section 4.2).

luminosity. For each bin, the error on the mean is calculated as the standard deviation of individual $\sigma^2_{\rm exc,L}$ divided by $\sqrt{N}$, where N is the number of sources in the bin (i.e., Equation (13) of Allevato et al. 2013; but note that a power index of 2 is missing in their summed term). The mean value in each bin can well represent the typical variability amplitude of the sources in the bin, despite the large error bars for individual sources (e.g., Allevato et al. 2013); the median has not been established to represent the typical variability amplitude. Spearman's test applied to the individual sources shows a significant anticorrelation between $\sigma^2_{\rm exc,L}$ and $L_{\rm X}$ (Spearman's $\rho = -0.31$, p-value $= 0.009$). This anticorrelation is mainly caused by the $\sigma^2_{\rm exc,L}$ difference between quasars ($L_{\rm X} > 10^{44}$ erg s^{-1}) and other AGNs. After removing quasars (only 19 sources), we find no significant relation between $L_{\rm X}$ and $\sigma^2_{\rm exc,L}$. There is also tentative evidence of an anticorrelation between $\sigma^2_{\rm exc,L}$ and $N_{\rm H}$: Spearman's $\rho = -0.23$, p-value $= 0.06$. However, this result might be a byproduct of the $\sigma^2_{\rm exc,L}$–$L_{\rm X}$ relation, since in our counts-limited sample (i.e., >600 net counts required) heavily obscured sources tend to be more luminous compared to less-obscured sources (see Figure 8). This interpretation is supported by the fact that no significant $\sigma^2_{\rm exc,L}$-$N_{\rm H}$ relation is found for luminosity-controlled samples ($L_{\rm X} \leqslant 10^{44}$ erg s^{-1} and $L_{\rm X} > 10^{44}$ erg s^{-1}).

The anticorrelation between $\sigma^2_{\rm exc,L}$ and $L_{\rm X}$ is unlikely to be a bias caused by the available counts since we are in a high S/N regime (see Section 3.2.5). Another bias might exist considering that we are probing generally shorter timescales for more luminous sources, since they have relatively high redshifts (see Figure 8), increasing the effects of time dilation. To test this point, we drop the first-epoch data for the low-redshift sample ($z < 2$, median $z = 1.0$), while keeping all data for the high-redshift sample ($z \geqslant 2$, median $z = 2.8$). Hence, the observed-frame total time spans are about 8 and 15 years for the low- and high-redshift samples, respectively (see Table 2). The median values of the rest-frame total time spans are both about 4 years [low-redshift: $8/(1+1.0)$, high-redshift: $15/(1+2.8)$]. We calculate $\sigma^2_{\rm exc,L}$ for this data set and find Spearman's $\rho = -0.29$, p-value $= 0.015$, similar to the results derived from the original data set. The results are also similar if we drop the fourth-epoch data instead of the first-epoch data for the low-redshift sample. We conclude that the anticorrelation between $\sigma^2_{\rm exc,L}$ and $L_{\rm X}$ is not caused by a bias of different rest-frame time spans. A bias might also arise from the fact that our observed-frame full energy band corresponds to different rest-frame energy bands. There is some evidence of energy-dependent variability reported in studies of Seyfert galaxies (e.g., Markowitz & Edelson 2004; Ponti et al. 2012). To estimate this effect, we fit the spectra of the rest-frame 2–10 keV band for each source. We calculate the luminosity excess standard deviation ($\sigma^2_{\rm exc,L,rest}$) and its uncertainty. The derived $\sigma^2_{\rm exc,L,rest}$ matches well with $\sigma^2_{\rm exc,L}$, with only six cases showing 2σ or higher deviation from $\sigma^2_{\rm exc,L,rest} = \sigma^2_{\rm exc,L}$, i.e.,

$$|\sigma^2_{\rm exc,L,rest} - \sigma^2_{\rm exc,L}| > 2\max(\delta\sigma^2_{\rm exc,L,rest},\ \delta\sigma^2_{\rm exc,L}), \quad (14)$$

where $\delta\sigma^2_{\rm exc,L,rest}$ and $\delta\sigma^2_{\rm exc,L}$ are the uncertainties of $\sigma^2_{\rm exc,L,rest}$ and $\sigma^2_{\rm exc,L}$, respectively. In agreement with $\sigma^2_{\rm exc,L}$, $\sigma^2_{\rm exc,L,rest}$ is also anticorrelated with $L_{\rm X}$: Spearman's $\rho = -0.30$, p-value $= 0.012$.

Several previous studies suggest that at a given luminosity level, sources at higher redshifts tend to have stronger X-ray variability (e.g., Almaini et al. 2000; Manners et al. 2002; Paolillo et al. 2004). To assess this point, we perform Spearman's test on $\sigma^2_{\rm exc,L}$ and redshifts for luminosity-controlled samples ($L_{\rm X} \leqslant 10^{44}$ erg s^{-1} and $L_{\rm X} > 10^{44}$ erg s^{-1}). The results show no significant correlation between $\sigma^2_{\rm exc,L}$ and redshift for both samples. However, the majority of the $L_{\rm X} \leqslant 10^{44}$ erg s^{-1} and $L_{\rm X} > 10^{44}$ erg s^{-1} sources are at $z \lesssim 2$ and $z \gtrsim 2$ (Figure 8), respectively. Thus, we cannot test the redshift dependence over a wide redshift range.

We do not find significant $\sigma^2_{\rm exc,N}$ dependence on $L_{\rm X}$, $N_{\rm H}$, or z for the 35 sources with $\sigma^2_{\rm exc,N}$ calculated (i.e., the sources with all four epochs having $\delta N_{{\rm H},i}/N_{{\rm H},i} < 0.4$).

3.2.7. Variability Dependence on Optical Spectral Type and Color

Type I AGNs have a higher $L_{\rm X}$ variable source fraction than their type II counterparts (83% versus 68%), likely due to their higher numbers of counts (Figure 2). Also, type I AGNs have a higher fraction of $N_{\rm H}$ variable sources (21% versus 14%). Figure 10 displays histograms of the $\sigma^2_{\rm exc,L}$ and $\sigma^2_{\rm exc,N}$ distributions for different optical spectral types. There are very few type I AGNs in the $\sigma^2_{\rm exc,N}$ histogram, because most type I AGNs are X-ray unobscured. For the $\sigma^2_{\rm exc,L}$ distributions, a KS test shows no apparent differences between type I and type II AGNs. Since optical spectral type is often related to the rest-frame optical color (e.g., $u - g$; see Section 2.2), we also check the $\sigma^2_{\rm exc,L}$ dependence on rest-frame $u - g$ color but do not find a significant relation. The similarity of long-term (years) X-ray variability between type I and type II AGNs has also been found by previous studies of both distant AGNs (e.g., Lanzuisi et al. 2014) and local Compton-thin Seyfert galaxies (e.g., Turner et al. 1997; Hernández-García et al. 2015), though Seyfert IIs tend to be less variable than Seyfert Is on short timescales (minutes to hours) (e.g., Turner et al. 1997; Awaki et al. 2006).

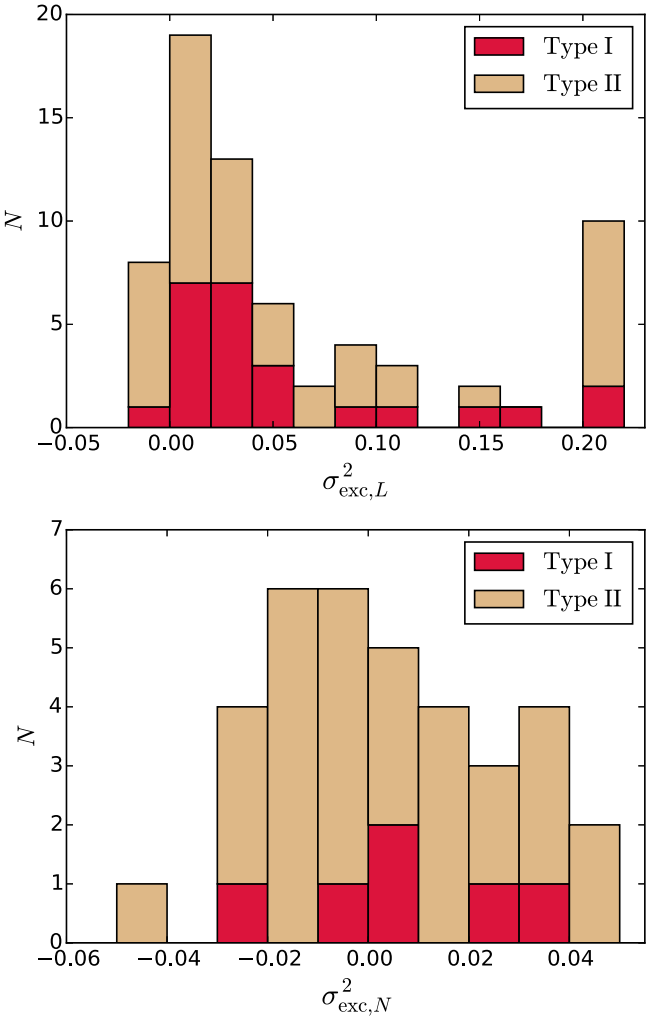

Figure 10. Upper panel: the $\sigma^2_{\rm exc,L}$ histogram. The red and brown colors indicate type I and type II AGNs, respectively. A KS test shows the dependence of $\sigma^2_{\rm exc,L}$ on optical type is not significant. The rightmost column indicates all sources with $\sigma^2_{\rm exc,L} > 0.2$. Lower panel: $\sigma^2_{\rm exc,N}$ histogram. Only the 35 sources with $\sigma^2_{\rm exc,N}$ calculated are shown here (Section 3.2.7). The rightmost column indicates all sources with $\sigma^2_{\rm exc,N} > 0.04$.

3.2.8. Variability Dependence on Timescale

Considering that our light curves are sparsely sampled (with four epochs), we cannot investigate the variability dependence on timescale for each source individually. Instead, we consider our entire sample as an ensemble and investigate its $L_{\rm X}$ ($N_{\rm H}$) variability on different timescales. We calculate the "structure function" (SF, i.e., ensemble-averaged fractional variability amplitude between two observations) as a function of rest-frame time interval ($\Delta t_{\rm rest}$).

First, for each epoch pair of a source (6 pairs in total for each source) we obtain a variability factor

$$f_v = \frac{\Delta x}{\overline{x}} = \frac{x_2 - x_1}{(x_2 + x_1)/2}; \quad (15)$$

and its uncertainty from error propagation

$$\delta f_v = \frac{x_1 x_2}{\overline{x}^2} \times \sqrt{\left(\frac{\delta x_1}{x_1}\right)^2 + \left(\frac{\delta x_2}{x_2}\right)^2}, \quad (16)$$

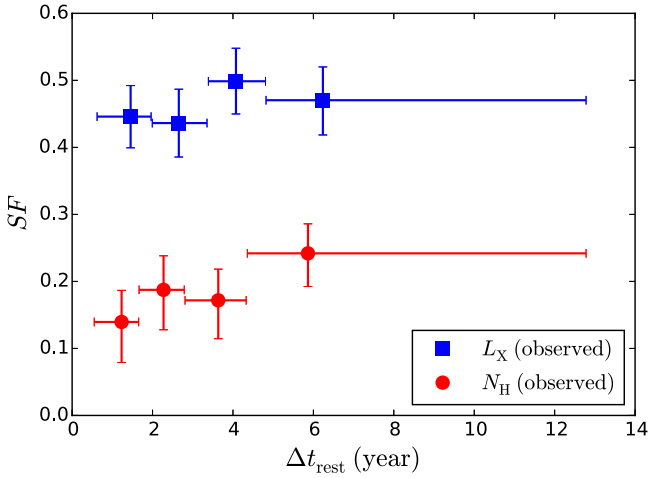

Figure 11. SFs as a function of rest-frame time interval, $\Delta t_{\rm rest}$. The blue squares and the red circles indicate the observed SFs for $L_{\rm X}$ and $N_{\rm H}$, respectively. The SF for $L_{\rm X}$ is calculated based on non-quasar ($L_{\rm X} < 10^{44}$ erg s^{-1}) sources only to avoid a bias (Section 3.2.8). The error bars of the SFs indicate 1σ uncertainties calculated from bootstrapping; the error bars of $\Delta t_{\rm rest}$ indicate the bin width.

where x_1 and x_2 are the best-fit $norm_i$ ($N_{{\rm H},i}$) of two different epochs; δx_1 and δx_2 are their 1σ errors. Each f_v is associated with a $\Delta t_{\rm rest}$ between two epochs. We then bin f_v with similar $\Delta t_{\rm rest}$ and calculate the SF (e.g., Vanden Berk et al. 2004) as

$$SF = \sqrt{\frac{\pi}{2}\langle |f_v| \rangle^2 - \langle (\delta f_v)^2 \rangle}, \quad (17)$$

where the angle brackets denote average values in the $\Delta t_{\rm rest}$ bin. We estimate the uncertainties of the SF from bootstrapping,[29] and the results are displayed in Figure 11.

Our 19 quasars generally have weaker variability (Section 3.2.6) and shorter $\Delta t_{\rm rest}$ (due to cosmological time dilation; see Figure 8). Hence, they might cause the $L_{\rm X}$ SF to be lower at shorter $\Delta t_{\rm rest}$. To avoid this bias, we do not include them when calculating the $L_{\rm X}$ SF. The resulting $L_{\rm X}$ SF is relatively flat as a function of timescale, with perhaps a suggestion of rising toward longer timescales.

The fractional variability amplitude of $N_{\rm H}$ is generally smaller than that of $L_{\rm X}$, and appears to increase as $\Delta t_{\rm rest}$ increases. In the $N_{\rm H}$ SF calculations, we only include the 35 sources with all four epochs having $\delta N_{{\rm H},i}/N_{{\rm H},i} < 0.4$ (Appendix A).

4. SUMMARY, DISCUSSION, AND FUTURE PROSPECTS

In this paper, we have performed long-term (up to ≈15 years, observed-frame) X-ray variability analyses for the 68 X-ray brightest radio-quiet AGNs in the uniquely deep CDF-S; most of these objects are at redshifts of 0.6–3.1, providing access to penetrating rest-frame X-rays up to ≈10–30 keV. AGNs like those studied here produce a significant fraction of cosmic accretion power; in this sense, they are the typical AGNs of the universe. We have performed both photometric and spectral variability analyses, and studied the dependence of variability on source properties and timescale. We summarize our main results in Section 4.1. In Section 4.2, we interpret the $L_{\rm X}$ variability in the context of

[29] We calculate the confidence interval as the range between the 16th and 84th percentiles.

AGN PSD. We present practical future extensions to this work in Section 4.3.

4.1. Summary of Main Results

The main results are the following:

1. Photometric analyses (Section 3.1) show that at above a 95% confidence level, 90% (61/68) and 16% (11/68) of our sources are variable in PF and HR, respectively. Our results confirm the prevalence of X-ray PF variability for typical AGNs in the distant universe (e.g., Paolillo et al. 2004; Lanzuisi et al. 2014). A large fraction of sources (~50%) is also found to be PF variable within single epochs. However, HR variability is generally insignificant within single epochs ($\lesssim$1 year, observed-frame).
2. Spectral analyses (using a *wabs* × *zwabs* × *pegpwrlw* model; see Section 3.2) demonstrate that the L_X- and N_H-variable source fractions are 74% (50/68) and 16% (11/68), respectively. Among the X-ray obscured quasars, the L_X-variable source fraction is also high (≈60%); this includes the BAL quasar (J033209.4–274806). Large-amplitude flux variability is rare; most sources (84%) have flux changes within a factor of two over 15 years (observed-frame, see Section 3.2.2). We do not find a significant anticorrelation between L_X and N_H variability, as might be expected for a photoionized absorber (see Section 3.2.4).
3. We have quantified the fractional variability scale by calculating the normalized excess variance (σ^2_{exc}) for each source (see Section 3.2.5). Quasars with $L_X > 10^{44}$ erg s^{-1} generally have smaller variability amplitudes than less luminous AGNs. We have not found any significant dependence of L_X variability amplitudes on optical spectral type, consistent with the results of Lanzuisi et al. (2014). Therefore, we appear to be observing the X-ray emission of most type II AGNs directly from the central engine; this can occur if X-rays are able to penetrate the obscuring material.
4. We have calculated SFs to illustrate the variability dependence on rest-frame timescale (Section 3.2.8). The L_X SF is relatively flat; the N_H SF appears to rise toward longer timescales.
5. A Compton-thick AGN candidate (Comastri et al. 2011) in our sample (J033218.3–275055) shows notable X-ray variability. Motivated by Comastri et al. (2011), we used a reflection-dominated *wabs* × *zwabs* × *pexmon* model to perform spectral analyses. The results indicate that both the reflection flux and the N_H are variable (see Appendix B). The variability timescale (≈ a year) indicates the size of the reflecting material is $\lesssim$0.3 pc. Nevertheless, it is also possible that the observed X-ray flux is a combination of both transmitted and reflected radiation, and the observed high-energy flux variability is mainly caused by the variable transmitted component.
6. We have identified a source in our sample (J033229.9–274530) that transitions from X-ray unobscured to obscured states over a ≈3 year rest-frame timescale (see Appendix C). The source is a type I object at $z = 1.21$ with $L_X \approx 7 \times 10^{43}$ erg s^{-1}. Its L_X is higher when it is less X-ray obscured. The angular size of an X-ray eclipsing cloud is estimated to be several degrees (viewed from the central SMBH). However, there is no corresponding optical spectral type transition, suggesting that the X-ray eclipsing material is too small to block most of the broad-line emission.

4.2. Interpretation from PSD

The observed low L_X variability amplitudes of quasars can be plausibly explained by the AGN PSD, which describes variability power as a function of frequency. An AGN PSD can often be well modeled as a broken power law (e.g., Uttley et al. 2002)

$$\mathrm{PSD}(\nu) = \begin{cases} \mathrm{PSD}_{\rm amp}\nu^{-1}, \text{ if } \nu < \nu_{\rm bf}; \\ \mathrm{PSD}_{\rm amp}\nu_{\rm bf}\nu^{-2}, \text{ if } \nu \geqslant \nu_{\rm bf}. \end{cases} \quad (18)$$

The normalization $\mathrm{PSD}_{\rm amp}$ is roughly constant (0.017 ± 0.006), according to studies of Seyfert galaxies (Papadakis 2004). The low-frequency power law extends at least to several year timescales in local Seyfert galaxies (e.g., Zhang 2011). $\nu_{\rm bf}$ is related to both SMBH mass ($M_{\rm BH}$) and bolometric luminosity ($L_{\rm bol}$) as (McHardy et al. 2006)

$$\begin{aligned} \nu_{\rm bf} &\sim 50\left(\frac{M_{\rm BH}}{10^8 M_\odot}\right)^{-2}\left(\frac{L_{\rm bol}}{10^{45}\ \mathrm{erg\ s^{-1}}}\right)\mathrm{yr^{-1}} \\ &\sim 10\left(\frac{L_X}{10^{44}\ \mathrm{erg\ s^{-1}}}\right)^{-1}\left(\frac{k_{\rm bol}}{50}\right)^{-1}\left(\frac{\lambda_{\rm Edd}}{0.1}\right)^{2}\mathrm{yr^{-1}}, \end{aligned} \quad (19)$$

where $\lambda_{\rm Edd}$ and $k_{\rm bol}$ are the Eddington ratio and bolometric correction factor for L_X (2–10 keV), respectively. Given a PSD of a source, the $\sigma^2_{{\rm exc},L}$ can be estimated as (e.g., Papadakis 2004; Papadakis et al. 2008)

$$\begin{aligned} \sigma^2_{{\rm exc},L} &= \int_{\nu_{\rm lf}}^{\nu_{\rm hf}} \mathrm{PSD}(\nu)d\nu \\ &= \mathrm{PSD}_{\rm amp}\ln\left(\frac{\nu_{\rm hf}}{\nu_{\rm lf}}\right), \text{ if } \nu_{\rm hf} < \nu_{\rm bf}. \end{aligned} \quad (20)$$

The integral bounds for our study are

$$\begin{aligned} \nu_{\rm lf} &\sim \frac{1+z}{t_{\rm span}} \text{ and} \\ \nu_{\rm hf} &\sim \frac{1+z}{t_{\rm bin}}, \end{aligned} \quad (21)$$

respectively, where $t_{\rm span} = 14.3$ years is the observed-frame total observation span and $t_{\rm bin} = 0.46$ year is the observed-frame median bin width of the four epochs. For an AGN with $L_X = 10^{44}$ erg s^{-1} and $\lambda_{\rm Edd} \sim 0.1$, the typical bolometric correction factor is $k_{\rm bol} \sim 50$ (e.g., Hopkins et al. 2007), and the typical redshift is ≈2 (see Figure 8). Thus, Equations (19) and (21) yield $\nu_{\rm bf} \sim \nu_{\rm hf} \sim 10$ yr^{-1}. For AGNs with higher luminosity (i.e., quasars), both $k_{\rm bol}$ and z tend to be larger. $\nu_{\rm hf}$ and $\nu_{\rm bf}$ will increase and decrease, respectively (assuming the same $\lambda_{\rm Edd}$); e.g., for a typical quasar at $z \sim 3$ with $L_X \sim 3 \times 10^{44}$ erg s^{-1} (see Figure 8), $\nu_{\rm bf}$ will increase by a factor of ~1.3 due to z, and $\nu_{\rm hf}$ will decrease at least three times due to L_X and $k_{\rm bol}$.[30] Therefore, $\nu_{\rm hf}$ is likely to

[30] The L_X (and related $k_{\rm bol}$) has a stronger effect than z. This is why we attribute L_X rather than z to be a major factor affecting variability in Section 3.2.6.

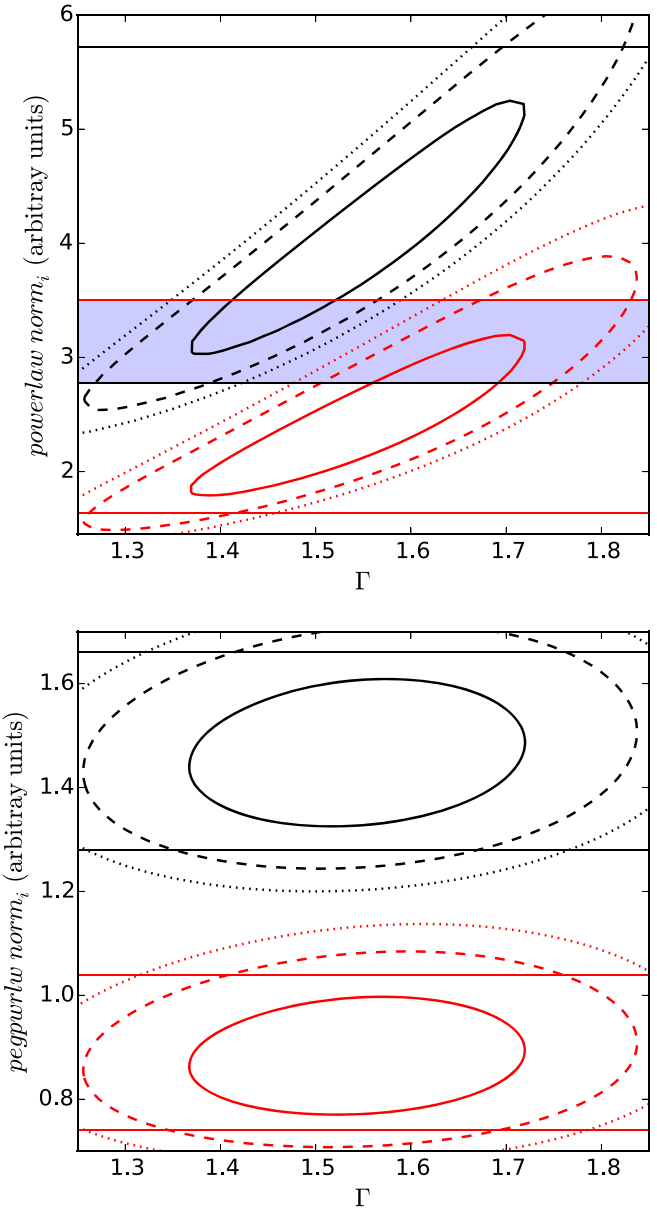

Figure 12. $norm_i - \Gamma$ confidence contours of the first two epochs of J033217.1–275220 resulting from modeling with *wabs* × *zwabs* × *powerlaw* (upper panel) and *wabs* × *zwabs* × *pegpwrlw* (lower panel). Black and red colors indicate epochs 1 and 2, respectively. The solid, dashed, and dotted curves indicate 1σ (68%), 2σ (95%), and 99% confidence contours, respectively. The horizontal solid lines indicate the 2σ uncertainty ranges of $norm_i$. In the upper panel, the 99% confidence contours do not overlap, indicating highly significant variability of $norm_i$ (i.e., >99.99% confidence level; see appendix A). However, the two projected $norm_i$ uncertainty ranges have an overlapping interval (blue shaded region), and a χ^2 test shows that the significance level of $norm_i$ variability is only 93%. Thus, the errors of $norm_i$ are overestimated under the assumption of constant Γ. In the lower panel, this issue does not occur.

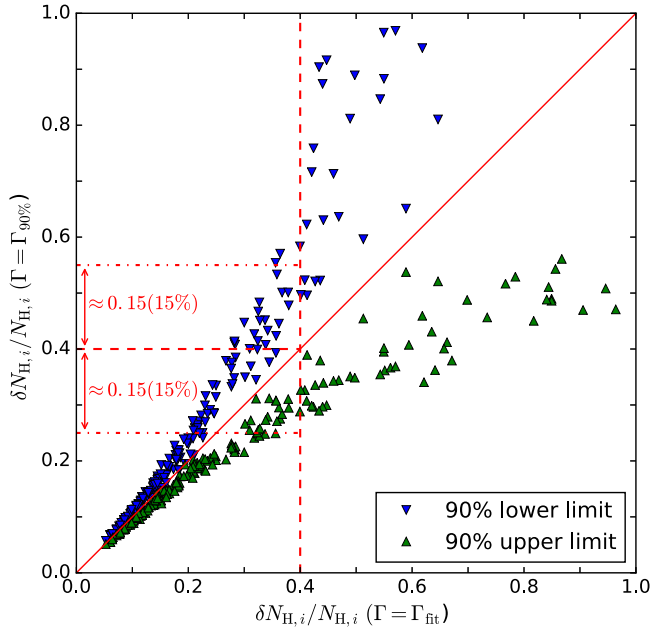

Figure 13. Fractional errors $\delta N_{\mathrm{H},i}/N_{\mathrm{H},i}$ obtained by fixing Γ at the 90% confidence limits of Γ_{fit} vs. those obtained by fixing Γ at the best-fit value. The green upward-pointing and blue downward-pointing triangles indicate the fractional errors obtained by fixing Γ at the upper and lower limits of Γ_{fit}, respectively. The red solid line indicates the ideal situation, i.e., the estimated fractional errors are not affected by fixing Γ at different values. The vertical red dashed line indicates our threshold, i.e., only sources with all four epochs having $\delta N_{\mathrm{H},i}/N_{\mathrm{H},i} < 0.4$ are included in the analyses where errors on $N_{\mathrm{H},i}$ are being used. Its intersection points with the approximate outer envelopes of the blue and green triangles are indicated by the horizontal red dash-dotted lines, and their deviations from $\delta N_{\mathrm{H},i}/N_{\mathrm{H},i} = 0.4$ (the horizontal red dashed line) are ≈0.15 (15%, as marked). Our sample consists 68 sources with each of them having 4 epochs. Thus, there are 272 (68 × 4) pairs of triangles plotted (though some are located out of the plotted ranges and are not shown). Note that for each source, the $\delta N_{\mathrm{H},i}/N_{\mathrm{H},i}$ (*x*-axis) are different for different epochs.

be higher than ν_{bf} for quasars (Equations (19) and (21)), i.e., the integral range in Equation (20) covers the power law with slope −2 that drops strongly toward high frequency. The resulting $\sigma_{\mathrm{exc,L}}$ for quasars should thus be smaller than for other AGNs, consistent with observations (Section 3.2.6). For a non-quasar AGN, we might be sampling only the low-frequency part of its PSD with slope −1 (i.e., $\nu_{\mathrm{hf}} < \nu_{\mathrm{bf}}$); Equations (20) and (21) result in an approximately constant $\sigma^2_{\mathrm{exc},L}$ value of 0.059 ± 0.021, regardless of source properties. This $\sigma^2_{\mathrm{exc},L}$ value is generally lower than the observed values for our non-quasar AGNs (see Figure 9), casting doubt on the universality of the constant-amplitude PSD model (e.g., Ponti et al. 2012; M. Paolillo et al., in preparation).

4.3. Future Work

Considering reasonably in-depth studies of the long-term X-ray variability of typical distant AGNs, it will be difficult to surpass greatly the present work for a considerable period of time; this is primarily due to the unmatched CDF-S exposure obtained over the extended period of ≈15 years. Additional X-ray variability studies should be done for the large population of X-ray fainter CDF-S AGNs (see Figure 8; e.g., X. C. Zheng et al., in preparation), although it will be more difficult to characterize these systems individually in depth. If *Chandra* continues to operate for another ≈10 years, as appears plausible (e.g., Wilkes 2015), obtaining additional CDF-S exposure in several years could lengthen our time baseline to up to ≈25 years in total. The *Advanced Telescope for High Energy Astrophysics* (*Athena*; e.g., Barcons et al. 2015), planned for launch in ≈13 years, has the best current prospects for substantially advancing long-term X-ray variability studies of typical AGNs in the distant universe. Owing to its greatly improved photon collecting area, it will obtain much better photon statistics for its deep-field AGNs. With suitable observation scheduling, it could efficiently perform a study similar to that in this work but for many more objects and with tens of epochs of observations

spanning a wide range of timescales. The prime deep-survey field for *Athena* is arguably the CDF-S, and *Athena* variability studies could build upon the long-term baseline of *Chandra* CDF-S observations utilized in this work.

We thank the referee for helpful feedback that improved this work. We thank Johannes Buchner, Michael Eracleous, Eric Feigelson, Brandon Kelly, Wanjun Liu, Kirpal Nandra, Michael Nowak, Piero Rosati, Paolo Tozzi, Phil Uttley, and Ningxiao Zhang for helpful discussions; and Scott Croom, Giorgio Lanzuisi, and James Mullaney for providing relevant data. G.Y., W.N.B., and F.V. acknowledge support from *Chandra* X-ray Center grant GO4-15130A. B.L. acknowledges support from National Natural Science Foundation of China grant 11673010 and Ministry of Science and Technology of China grant 2016YFA0400702. Y.Q.X., M.Y.S., and X.C.Z. acknowledge support from the National Thousand Young Talents program, the 973 Program (2015CB857004), NSFC-11473026, NSFC-11421303, the Strategic Priority Research Program "The Emergence of Cosmological Structures" of the Chinese Academy of Sciences (XDB09000000), the CAS Frontier Science Key Research Program (QYZDJ-SSW-SLH006), and the Fundamental Research Funds for the Central Universities. F.E.B. and S. Schulze acknowledge support from CONICYT-Chile grants Basal-CATA PFB-06/2007 and the Ministry of Economy, Development, and Tourism's Millennium Science Initiative through grant IC120009, awarded to The Millennium Institute of Astrophysics, MAS. Furthermore, F.E.B. acknowledges support from FONDECYT Regular 1141218 and "EMBIGGEN" Anillo ACT1101, and S. Schulze acknowledges support from FONDECYT grant 3140534. S. Kim acknowledges support from FONDECYT grant 3130488. J.X.W. acknowledges support from NSFC 11233002 and the 973 program 2015CB857005. This research has made use of Astropy, a community developed core Python package for Astronomy (Astropy Collaboration, 2013), and the VizieR catalog access tool, CDS, Strasbourg, France.

APPENDIX A
ERROR ESTIMATION OF MODEL PARAMETERS

As described in Section 3.2.1, we fit spectra of the four epochs simultaneously with a *wabs* × *zwabs* × *pegpwrlw* model. The photon index, Γ, is linked across the four epochs, assuming no Γ variability (see Section 3.2.1 for the justification of this assumption). In this appendix, we first explain our choice of *pegpwrlw* over *powerlaw*, and then describe our method to estimate the errors of $N_{\mathrm{H},i}$.

As an illustrative example, we show the $norm_i$-Γ confidence contours of the first two epochs of J033217.1–275220 resulting from fitting with a model of *wabs* × *zwabs* × *powerlaw* (see the upper panel of Figure 12). The contours, as expected, show positive correlations between $norm_i$ and Γ. Since no overlapping region exists between the two 99% confidence contours, the probability of the two epochs having both the same $norm_i$ and Γ is very low [$<(1\%–99\%)^2 = 0.01\%$]. Therefore, the $norm_i$ variability must be very significant ($>1\%–0.01\% = 99.99\%$) under our assumption of constant Γ. However, if we evaluate the $norm_i$ variability by checking the one-dimensional (1D) errors (2σ) of $norm_i$ (the projected range on the *y*-axis), the variability seems to be less significant due to the existence of an overlapping interval (blue shaded region). More quantitatively,

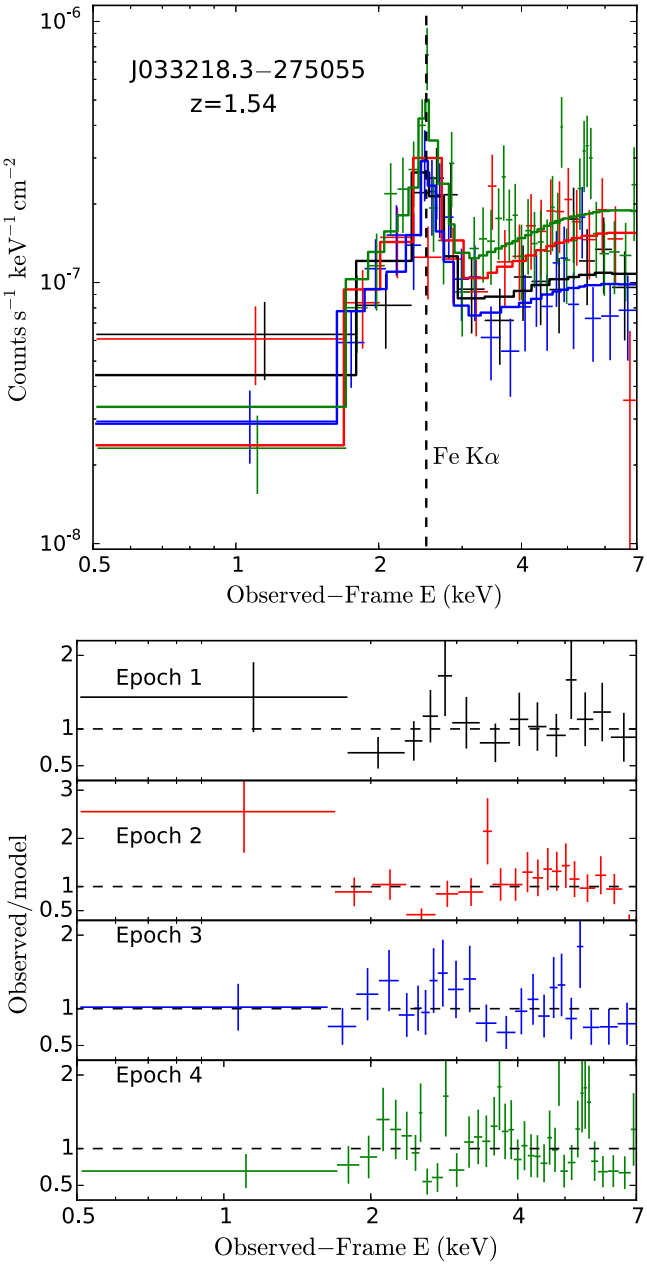

Figure 14. Upper panel: unfolded (i.e., intrinsic) spectra for the Compton-thick candidate J033218.3–275055 using fitting model *wabs* × *zwabs* × *pexmon*. The solid lines indicate best-fit model photon flux density. Different colors indicate different epochs. The vertical dashed line indicates the energy of Fe Kα line (i.e., rest-frame 6.4 keV). Data are binned for display purposes only. Note that the flux in the high-energy band (less affected by absorption) varies significantly. Lower panel: ratio of observed and model photon flux.

if we perform a χ^2 test of the $norm_i$ variability using the best-fit values and 1D errors, the resulting significance of variability is only 93%. This apparent discrepancy occurs because when calculating the 1D errors of $norm_i$ by projecting the 2D contours, the positive $norm_i - \Gamma$ correlations and our underlying assumption of constant Γ are "forgotten." This is evident since the blue shaded region only covers the two dashed contours at very different Γ, i.e., the same $norm_i$ can be achieved only when the assumption of constant Γ is violated. Reading Figure 12, Γ would need to change by $\Delta\Gamma \approx 0.2$–0.3, and this is larger than any physically expected Γ change (see Section 3.2.1). Therefore, the errors of $norm_i$ are overestimated under this

Table 4
Spectral Fitting[a] Results of the Compton-thick Candidate (J033218.3–275055)

Epoch	Γ	$N_{\rm H}$ (10^{22} cm^{-2})	Flux[b] (10^{-15} erg cm^{-2} s^{-1})
1	1.80	$5.61^{+2.88}_{-2.38}$	$4.16^{+0.34}_{-0.40}$
2	⋯	$17.00^{+4.80}_{-4.40}$	$5.47^{+0.44}_{-0.46}$
3	⋯	$7.81^{+2.89}_{-2.52}$	$3.71^{+0.26}_{-0.26}$
4	⋯	$17.80^{+3.60}_{-3.30}$	$6.64^{+0.33}_{-0.35}$

Note.
[a] The spectral fitting model is *wabs* × *zwabs* × *pexmon* (see Section B).
[b] Full-band (0.5–7 keV) model flux, not corrected for Galactic or intrinsic absorption.

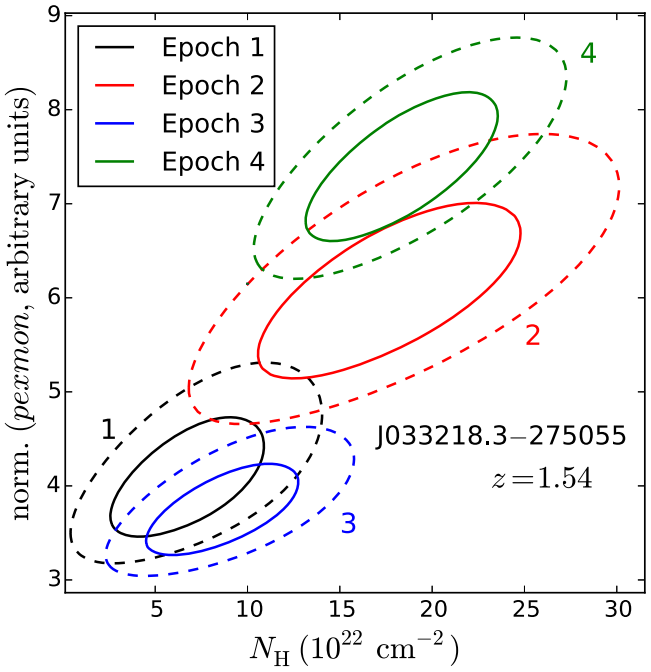

Figure 15. Confidence contours of the normalizations of *pexmon* and $N_{\rm H}$ for source J033218.3–275055, the Compton-thick candidate. The solid and dashed curves indicate 1σ and 2σ confidence contours, respectively. Different colors indicate different epochs, and the epoch indexes are also labeled beside the corresponding contours.

assumption of constant Γ. This problem is prevalent when using *powerlaw*, since positive correlations exist for almost all sources. However, the positive correlations can be mostly eliminated by replacing *powerlaw* with *pegpwrlw* (see the lower panel of Figure 12). *pegpwrlw* differs from *powerlaw* by having its normalization based on intrinsic flux in a given finite band rather than the flux density at observed-frame 1 keV. We find that setting the normalization band as $E_{\rm peg}-7$ keV produces nearly horizontal $norm_i$-Γ contours for all sources, where E_{peg} is the minimum between 0.5 keV and the observed-frame e-folding energy ($E_{\rm fold}$) caused by intrinsic photoelectric absorption. Technically, we obtain the photoelectric cross section $\sigma_{\rm photo}$ as a function of energy (Morrison & McCammon 1983), and solve the equation $\langle N_{\rm H}\rangle \times \sigma_{\rm photo}[E_{\rm fold}\times(1+z)]=1$ to obtain $E_{\rm fold}$,[31] where the factor $1+z$ is to convert observed-frame to rest-frame energy.

[31] We first fit the spectrum using an arbitrary normalization band and calculate the $\langle N_{\rm H}\rangle$ from the best-fit $N_{{\rm H},i}$. The best-fit $N_{{\rm H},i}$ is independent of the exact choice of energy band.

Similar positive correlations are also, as expected, prevalent in the $N_{{\rm H},i}$-Γ contours. However, we are not aware of any model choices that can eliminate these correlations (as for the choice of *pegpwrlw* in the $norm_i$ case). Alternatively, if intrinsic Γ ($\Gamma_{\rm intr}$) were given, one could fix $\Gamma=\Gamma_{\rm intr}$ and estimate the the errors of $N_{{\rm H},i}$. But in reality, $\Gamma_{\rm intr}$ is not perfectly known. We thus adopt an approximation, i.e., fixing $\Gamma=\Gamma_{\rm fit}$. The idea is to approximate $\Gamma_{\rm intr}$ as $\Gamma_{\rm fit}$. Admittedly, compared to fixing $\Gamma=\Gamma_{\rm intr}$, this approximation might overestimate or underestimate the errors of $N_{{\rm H},i}$. To evaluate this possible issue, we fix Γ at the 90% confidence lower and upper limits of $\Gamma_{\rm fit}$, respectively, and then estimate the errors. The lower and upper limits approximate the boundaries of possible $\Gamma_{\rm intr}$ values. If fixing Γ at these boundaries results in similar errors as fixing Γ at $\Gamma_{\rm fit}$, we conclude that our approximation (i.e., fixing $\Gamma=\Gamma_{\rm fit}$) gives accurate errors of $N_{{\rm H},i}$ for a given source. Figure 13 shows the results. The dependence of estimated fractional error $\delta N_{{\rm H},i}/N_{{\rm H},i}$ on Γ is stronger when the error is larger. In Figure 13, at $\delta N_{{\rm H},i}/N_{{\rm H},i}=0.4$ (the vertical dashed line), fixing Γ at its 90%-confidence lower and upper limits of $\Gamma_{\rm fit}$ results in $\delta N_{{\rm H},i}/N_{{\rm H},i}\lesssim 0.55$ and $\gtrsim$0.25, respectively (the dashed–dotted lines). Since $\Gamma_{\rm intr}$ is very likely within the range of the 90% limits of $\Gamma_{\rm fit}$, fixing $\Gamma=\Gamma_{\rm intr}$ (if it were perfectly known) should give $\delta N_{{\rm H},i}/N_{{\rm H},i}$ within the range of ≈0.25–0.55. Therefore, fixing $\Gamma=\Gamma_{\rm intr}$ would lead to $\delta N_{{\rm H},i}/N_{{\rm H},i}$ deviating from that obtained by our approximation (fixing $\Gamma=\Gamma_{\rm fit}$) by $\lesssim$15% (i.e., $15\%=0.15=0.55-0.4=0.4-0.25$). For epochs with $\delta N_{{\rm H},i}/N_{{\rm H},i}<0.4$, this value should be even lower. In the analyses where errors on $N_{{\rm H},i}$ are being used (Sections 3.2.6 and 3.2.8), we only include the 35 sources with all four epochs having $\delta N_{{\rm H},i}/N_{{\rm H},i}<0.4$. This criterion guarantees that the $N_{{\rm H},i}$ fractional errors estimated by fixing $\Gamma=\Gamma_{\rm fit}$ differ from those estimated by fixing $\Gamma=\Gamma_{\rm intr}$ by $\lesssim$15%. Though not ideal, this criterion is a practical solution for our $N_{\rm H}$ variability analyses, balancing the accuracy of error estimation and the sample size.

APPENDIX B
A HIGHLY VARIABLE COMPTON-THICK CANDIDATE

J033218.3–275055 is a bright Compton-thick candidate AGN at $z=1.54$ reported in the literature (Tozzi et al. 2006; Comastri et al. 2011). It is classified as an optical type II object. It shows a strong Fe Kα emission line with a rest-frame equivalent width (REW) of ≈1.2 keV (Comastri et al. 2011). Our spectral fitting confirms its highly obscured nature ($N_{\rm H}=3\times10^{23}$ cm^{-2}). Both its $L_{\rm X}$ and $N_{\rm H}$ values are variable ($\Delta{\rm AIC}_L=38$ and $\Delta{\rm AIC}_N=5.1$). However, its high *goodness* (44%) and low Γ (1.2, i.e., our allowed lower limit, see Section 3.2.1) indicate the model *wabs* × *zwabs* × *pegpwrlw* is likely inappropriate (see Figure 6). Thus, motivated by Comastri et al. (2011), we use the model *wabs* × *zwabs* × *pexmon* (for *pexmon*, see Magdziarz & Zdziarski 1995; Nandra et al. 2007) to fit the data. We set the *pexmon* model to be fully reflection dominated and fix the inclination angle at 60°. We link the Γ (*pexmon*) of all four epochs, and set $norm_i$ (*pexmon*) and $N_{{\rm H},i}$ (*zwabs*) free (not linked). The fitted spectra of the reflection-dominated model are shown in Figure 14, and the detailed fitting results are presented in Table 4.

Despite having the same number of degrees of freedom as the previous model (*wabs* × *zwabs* × *pegpwrlw*), the new fitting results in a *goodness* = 8% and best-fit $\Gamma=1.80$, values that are

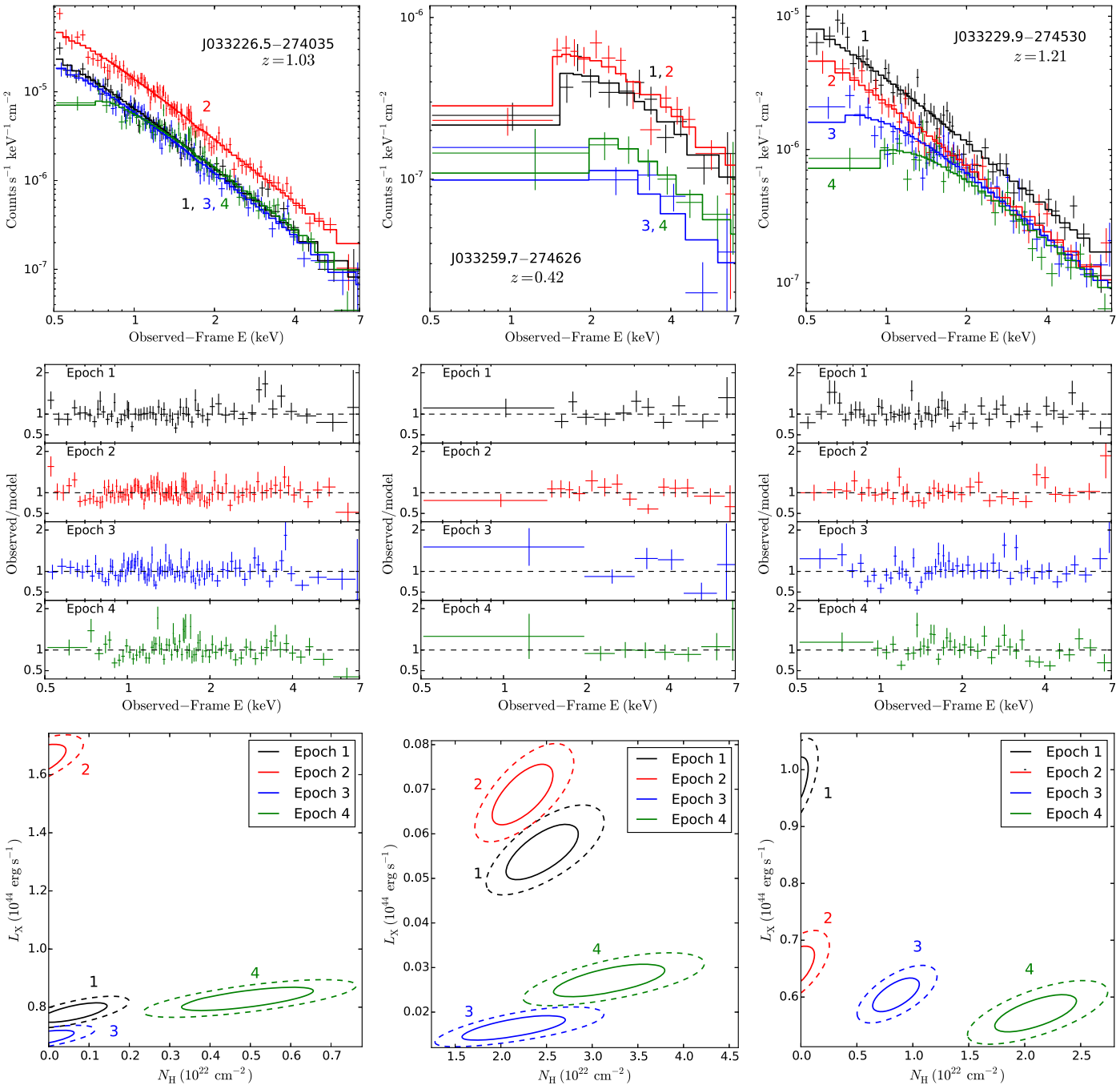

Figure 16. Upper panels: unfolded (i.e., intrinsic) spectra for J033226.5–274035, J033259.7–274626, and J033229.9–274530, respectively. The solid lines indicate best-fit model photon flux. Different colors indicate different epochs, and the epoch indexes are also labeled beside the corresponding spectra. Data are binned for display purposes only. Middle panels: the corresponding ratios of observed and model photon flux density. Lower panels: the corresponding L_X–N_H confidence contours. J033226.5–274035 has significantly higher luminosity in epoch 2. The luminosity of J033259.7–274626 drops by a large factor (≈3) since epoch 3. For J033229.9–274530, the spectral shape changes obviously among epochs.

more common among the *goodness* and Γ distributions for our overall sample (see Figure 6). Also, the new model has AIC much smaller than the previous model (ΔAIC = 54), indicating a significant improvement in the fit quality. Thus, we consider this reflection-dominated model to be more physically plausible than the simple transmission-dominated model. Following Section 2.4.1 of Nandra et al. (2007), this Γ value (i.e., 1.80) results in an REW of Fe Kα (*pexmon*) of ≈1.4 keV, consistent with Comastri et al. (2011). Similar to the approach in Section 3.2.3, we test the significance of reflection flux and N_H variability by linking $norm_i$ (*pexmon*) and $N_{H,i}$, respectively. The increased AIC values (i.e., 39 and 4.2) are both greater than 4, indicating both the reflection flux and N_H are variable (Section 3.2.3). The confidence contours are shown in Figure 15. Both the absorption and continuum are weak in epoch 1; they rise in epoch 2 and then drop in epoch 3; in epoch 4, they rise again. The amplitude of flux variability is large; e.g., the flux in epoch 4 is almost twice that in epochs 1 and 3. The variability timescale (≈ a year) constrains the size of the reflecting material to be $\lesssim$0.3 pc.

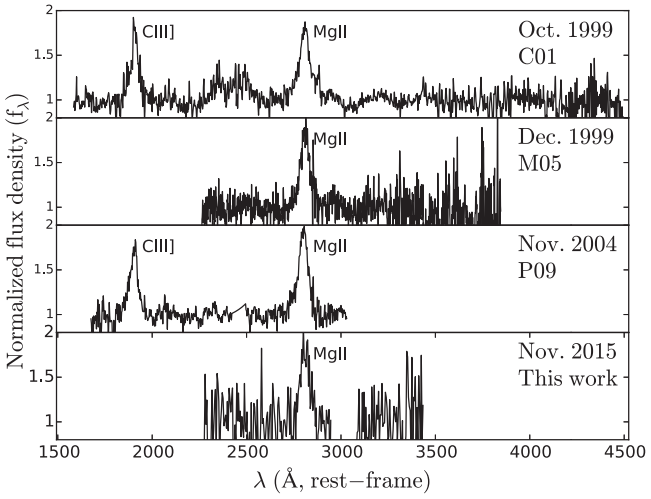

Figure 17. Normalized optical spectra of J033229.9–274530 at $z = 1.21$. The observation dates and the references are listed in the upper-right corner of each panel (C01: Croom et al. 2001; M05: Mignoli et al. 2005; P09: Popesso et al. 2009). The Mg II λ2798 broad emission line is present in all four spectra.

However, there is a possible alternative explanation for the observed high-energy flux variability of this source, though our reflection-dominated model explains the data satisfactorily. The observed X-ray emission might be a combination of both transmitted and reflected radiation. In this scenario, the transmission component is variable and results in the observed high energy flux variability, while the reflection component is stable. To test this scenario, we use a *wabs* × *zwabs* × (*pegpwrlw* + *pexmon*) model. We assume that the *pegpwrlw* and *pexmon* components share the same non-variable Γ, and the normalization of *pexmon* is the same across epochs. The $N_{\rm H}$ (*zwabs*) and the normalization of *pegpwrlw* are allowed to vary across epochs. Other parameters of the *pexmon* component are the same as for the reflection-dominated model. This composite model yields $\Gamma = 1.5$ and *goodness* = 5%, similar to that of the reflection-dominated model. The resulting transmitted flux almost completely shuts down at epoch 1 and epoch 3 (more than an order of magnitude smaller than at epoch 2 and epoch 4). Such strong variability is not likely to be realistic, considering the general variability amplitudes of our sources (see Section 3.2.2). Nevertheless, more complex transmission-reflection hybrid models might produce more physically plausible results, though they cannot be constrained well owing to the available number of counts.

APPENDIX C
THREE SIGNIFICANTLY VARIABLE SOURCES

As illustrative examples, we investigate three significantly variable sources. The first source, J033226.5–274035 ($z = 1.03$), is our brightest source; it also has the most significant $L_{\rm X}$ variability. The second source, J033259.7–274626 ($z = 0.42$), is also $L_{\rm X}$-variable, but has counts typical in our sample; this source is shown as a representative sample member. The third source, J033229.9–274530 ($z = 1.21$), has the most significant $N_{\rm H}$ variability; it transitions from an X-ray unobscured to obscured state. Their fitted spectra and $L_{\rm X}$–$N_{\rm H}$ confidence contours are shown in Figure 16.

J033226.5–274035 has the largest number of total net counts (≈11000). It has $\Delta{\rm AIC}_L = 1059$ and $\Delta{\rm AIC}_N = 15$, indicating both $L_{\rm X}$ and $N_{\rm H}$ variability. The $\Delta{\rm AIC}_L$ is the largest among those of our sources. Its $L_{\rm X}$ in the second epoch is about two times the $L_{\rm X}$ in the other epochs. Its $N_{\rm H}$ is generally low: $N_{\rm H}$ only has upper limits in the first three epochs and rises to $\approx 4 \times 10^{21}$ cm^{-2} in the last epoch. J033226.5–274035 and another bright (net counts ≈6500) and variable source ($\Delta{\rm AIC}_L = 38$, $\Delta{\rm AIC}_N = 5.1$), J033218.3–275055, are also identified as optically variable sources by Falocco et al. (2015) based on their *r*-band variability.

J033259.7–274626 has total net counts of ≈1300, similar to the median counts of our sample (1399). It has $\Delta{\rm AIC}_L = 165$, indicating significant $L_{\rm X}$ variability. Its $L_{\rm X}$ values in the first two epochs are about three times higher than those in the last two epochs. It is X-ray obscured (i.e., $N_{\rm H} > 10^{22}$ cm^{-2}) with no significant $N_{\rm H}$ variability detected ($\Delta{\rm AIC}_N = -0.9$).

J033229.9–274530 has $\Delta{\rm AIC}_L = 144$ and $\Delta{\rm AIC}_N = 83$ with a total net counts of ≈5000. It is the most significantly $N_{\rm H}$ variable source (i.e., has maximum $\Delta{\rm AIC}_N$). The $N_{\rm H}$ values in the first two epochs are low (consistent with zero). The $N_{\rm H}$ rises in epoch 3 and reaches $\approx 2 \times 10^{22}$ cm^{-2} in epoch 4. Its $L_{\rm X}$ in epoch 1 is ≈2 times higher than $L_{\rm X}$ in the other epochs. The X-ray type transition happens between epochs 2 and 4, and thus corresponds to a rest-frame timescale $t_{\rm tran} \sim 3$ year. If we interpret the transition as an "eclipse" event, this long timescale indicates the eclipsing material is located at a distance larger than that of the BLR from the central engine. This is because BLR-cloud eclipses are likely to happen on much shorter timescales (hours to days; e.g., Maiolino et al. 2010; Wang et al. 2010). Assuming that the eclipsing material is in a single "cloud" within the inner torus region, its distance (r) from the central engine is ∼0.1 pc.[32] Applying Kepler's third law, we can calculate its orbital period

$$t_{\rm orbit} = 2\pi \frac{r^{\frac{3}{2}}}{(M_{\rm BH} G)^{\frac{1}{2}}} \sim 300 \left(\frac{M_{\rm BH}}{10^8\, M_\odot}\right)^{-\frac{1}{2}} \text{year}. \quad (22)$$

Then we can estimate the angular size of the cloud, θ (viewed from the central SMBH), as

$$\theta \sim \frac{t_{\rm tran}}{t_{\rm orbit}} \times 360^\circ \sim 4^\circ \left(\frac{M_{\rm BH}}{10^8\, M_\odot}\right)^{\frac{1}{2}}. \quad (23)$$

To investigate if the optical spectral type also changes, we have compiled three optical spectra from the literature (Croom et al. 2001; Mignoli et al. 2005; Popesso et al. 2009) and obtained a new spectrum on 2015 November 8. The new observation was performed using the IMACS Short-Camera of the 6.5 m *Magellan* Telescope. The four spectra are presented in Figure 17. In all four spectra, the broad Mg II λ2798 line is detected. In the first and third spectra, the C III] λ1909 line is also detected.[33] Thus, the optical spectral type of this source remains type I in all four spectra. The lack of optical spectral

[32] The distance is estimated from the empirical relation between the inner torus radius and X-ray luminosity obtained from dust reverberation-mapping studies (Koshida et al. 2014).

[33] We do not perform quantitative analyses, since all of the spectra cannot be reduced uniformly.

type transitions indicates the X-ray eclipsing material is not large enough to block most emission from the BLR. This result is consistent with recent studies of optical spectral type transition AGNs that suggest significant changes (~10 times) in luminosity as the main cause of transitions (e.g., LaMassa et al. 2015; Runnoe et al. 2016).

REFERENCES

Abdo, A. A., Ackermann, M., Ajello, M., et al. 2010, ApJ, 722, 520
Aird, J., Coil, A. L., Georgakakis, A., et al. 2015, MNRAS, 451, 1892
Akaike, H. 1974, ITAC, 19, 716
Allevato, V., Paolillo, M., Papadakis, I., & Pinto, C. 2013, ApJ, 771, 9
Almaini, O., Lawrence, A., Shanks, T., et al. 2000, MNRAS, 315, 325 (A00)
Arévalo, P., Bauer, F. E., Puccetti, S., et al. 2014, ApJ, 791, 81
Arnaud, K. A. 1996, in ASP Conf. Ser. 101, Astronomical Data Analysis Software and Systems V, ed. G. H. Jacoby & J. Barnes (San Francisco, CA: ASP), 17
Awaki, H., Murakami, H., Ogawa, Y., & Leighly, K. M. 2006, ApJ, 645, 928
Barcons, X., Nandra, K., Barret, D., et al. 2015, JPhCS, 610, 012008
Barger, A. J., Cowie, L. L., Capak, P., et al. 2003, AJ, 126, 632
Bauer, F. E., Arévalo, P., Walton, D. J., et al. 2015, ApJ, 812, 116
Begelman, M. C., Fabian, A. C., & Rees, M. J. 2008, MNRAS, 384, L19
Bonzini, M., Padovani, P., Mainieri, V., et al. 2013, MNRAS, 436, 3759
Brandt, W. N., Fabian, A. C., Takahashi, K., et al. 1997, MNRAS, 290, 617
Brightman, M., Silverman, J. D., Mainieri, V., et al. 2013, MNRAS, 433, 2485
Broos, P. S., Townsley, L. K., Feigelson, E. D., et al. 2010, ApJ, 714, 1582
Buchner, J., Georgakakis, A., Nandra, K., et al. 2014, A&A, 564, A125
Burnham, K. P., & Anderson, D. R. 2002, Model Selection and Multimodel Inference: a Practical Information-theoretic Approach (New York: Springer-Verlag)
Cash, W. 1979, ApJ, 228, 939
Chartas, G., Saez, C., Brandt, W. N., Giustini, M., & Garmire, G. P. 2009, ApJ, 706, 644
Civano, F., Marchesi, S., Comastri, A., et al. 2016, ApJ, 819, 62
Collinge, M. J., Brandt, W. N., Kaspi, S., et al. 2001, ApJ, 557, 2
Comastri, A., Ranalli, P., Iwasawa, K., et al. 2011, A&A, 526, L9
Connolly, S. D., McHardy, I. M., Skipper, C. J., & Emmanoulopoulos, D. 2016, MNRAS, 459, 3963
Corral, A., Georgantopoulos, I., Watson, M. G., et al. 2015, A&A, 576, A61
Croom, S. M., Warren, S. J., & Glazebrook, K. 2001, MNRAS, 328, 150
Falocco, S., Paolillo, M., Covone, G., et al. 2015, A&A, 579, A115
Fausnaugh, M. M., Denney, K. D., Barth, A. J., et al. 2016, ApJ, 821, 56
Filiz, Ak. N., Brandt, W. N., Hall, P. B., et al. 2013, ApJ, 777, 168
Gallagher, S. C., Brandt, W. N., Chartas, G., et al. 2006, ApJ, 644, 709
Gallagher, S. C., Brandt, W. N., Chartas, G., & Garmire, G. P. 2002, ApJ, 567, 37
Gallagher, S. C., Brandt, W. N., Wills, B. J., et al. 2004, ApJ, 603, 425
Garmire, G. P., Bautz, M. W., Ford, P. G., Nousek, J. A., & Ricker, G. R., Jr. 2003, Proc. SPIE, 4851, 28
Gehrels, N. 1986, ApJ, 303, 336
George, I. M., Turner, T. J., Yaqoob, T., et al. 2000, ApJ, 531, 52
Gibson, R. R., & Brandt, W. N. 2012, ApJ, 746, 54 (G12)
Gibson, R. R., Brandt, W. N., & Schneider, D. P. 2008, ApJ, 685, 773
Gibson, R. R., Jiang, L., Brandt, W. N., et al. 2009, ApJ, 692, 758
Goodrich, R. W. 1995, ApJ, 440, 141
Hernández-García, L., Masegosa, J., González-Martín, O., & Márquez, I. 2015, A&A, 579, A90
Hewett, P. C., & Foltz, C. B. 2003, AJ, 125, 1784
Hickox, R. C., Mullaney, J. R., Alexander, D. M., et al. 2014, ApJ, 782, 9
Hopkins, P. F., Richards, G. T., & Hernquist, L. 2007, ApJ, 654, 731
Hsu, L.-T., Salvato, M., Nandra, K., et al. 2014, ApJ, 796, 60
Iwasawa, K., Vignali, C., Comastri, A., et al. 2015, A&A, 574, A144
Just, D. W., Brandt, W. N., Shemmer, O., et al. 2007, ApJ, 665, 1004
Kara, E., Fabian, A. C., Cackett, E. M., et al. 2013, MNRAS, 428, 2795
Kelly, B. C., Bechtold, J., Siemiginowska, A., Aldcroft, T., & Sobolewska, M. 2007, ApJ, 657, 116
Khachikian, E. Y., & Weedman, D. W. 1974, ApJ, 192, 581
King, A., & Pounds, K. 2015, ARA&A, 53, 115
Koshida, S., Minezaki, T., Yoshii, Y., et al. 2014, ApJ, 788, 159
Krolik, J. H., & Kriss, G. A. 1995, ApJ, 447, 512
LaMassa, S. M., Cales, S., Moran, E. C., et al. 2015, ApJ, 800, 144
Lanzuisi, G., Ponti, G., Salvato, M., et al. 2014, ApJ, 781, 105 (L14)
Luo, B., Brandt, W. N., Xue, Y. Q., et al. 2010, ApJS, 187, 560
Magdziarz, P., & Zdziarski, A. A. 1995, MNRAS, 273, 837
Maiolino, R., Risaliti, G., Salvati, M., et al. 2010, A&A, 517, A47
Manners, J., Almaini, O., & Lawrence, A. 2002, MNRAS, 330, 390
Mao, M. Y., Sharp, R., Norris, R. P., et al. 2012, MNRAS, 426, 3334
Markowitz, A., & Edelson, R. 2004, ApJ, 617, 939
Markowitz, A., Edelson, R., & Vaughan, S. 2003, ApJ, 598, 935
Markowitz, A. G., Krumpe, M., & Nikutta, R. 2014, MNRAS, 439, 1403
Matt, G., Bianchi, S., Guainazzi, M., et al. 2011, A&A, 533, A1
Matt, G., Guainazzi, M., & Maiolino, R. 2003, MNRAS, 342, 422
McHardy, I. M., Koerding, E., Knigge, C., Uttley, P., & Fender, R. P. 2006, Natur, 444, 730
Mignoli, M., Cimatti, A., Zamorani, G., et al. 2005, A&A, 437, 883
Miller, B. P., Brandt, W. N., Schneider, D. P., et al. 2011, ApJ, 726, 20
Miniutti, G., Brandt, W. N., Schneider, D. P., et al. 2012, MNRAS, 425, 1718
Morrison, R., & McCammon, D. 1983, ApJ, 270, 119
Mullaney, J., Del-Moro, A., Aird, J., et al. 2015, ApJ, 808, 184
Nandra, K., George, I. M., Mushotzky, R. F., Turner, T. J., & Yaqoob, T. 1997, ApJ, 476, 70
Nandra, K., O'Neill, P. M., George, I. M., & Reeves, J. N. 2007, MNRAS, 382, 194
Netzer, H. 2015, ARA&A, 53, 365
Norman, C., Hasinger, G., Giacconi, R., et al. 2002, ApJ, 571, 218
Ogasaka, Y., Inoue, H., Brandt, W. N., et al. 1997, PASJ, 49, 179
Paolillo, M., Schreier, E. J., Giacconi, R., Koekemoer, A. M., & Grogin, N. A. 2004, ApJ, 611, 93 (Pao04)
Papadakis, I. E. 2004, MNRAS, 348, 207
Papadakis, I. E., Chatzopoulos, E., Athanasiadis, D., Markowitz, A., & Georgantopoulos, I. 2008, A&A, 487, 475 (Pap08)
Peterson, B. 2014, SSRv, 183, 253
Peterson, B. M. 2001, in Advanced Lectures on the Starburst-AGN Connection, ed. I. Aretxaga, D. Kunth, & R. Mújica (Singapore: World Scientific), 3
Ponti, G., Papadakis, I., Bianchi, S., et al. 2012, A&A, 542, A83
Popesso, P., Dickinson, M., Nonino, M., et al. 2009, A&A, 494, 443
Pounds, K. A., Reeves, J. N., Page, K. L., Wynn, G. A., & O'Brien, P. T. 2003, MNRAS, 342, 1147
Puccetti, S., Comastri, A., Bauer, F. E., et al. 2016, A&A, 585, A157
Puccetti, S., Comastri, A., Fiore, F., et al. 2014, ApJ, 793, 26
Ranalli, P., Comastri, A., Vignali, C., et al. 2013, A&A, 555, A42
Ravikumar, C. D., Puech, M., Flores, H., et al. 2007, A&A, 465, 1099
Reynolds, C. S. 1997, MNRAS, 286, 513
Ricci, C., Bauer, F. E., Arevalo, P., et al. 2016, ApJ, 820, 5
Richards, G. T., Fan, X., Newberg, H. J., et al. 2002, AJ, 123, 2945
Risaliti, G., Elvis, M., Fabbiano, G., et al. 2007, ApJL, 659, L111
Risaliti, G., Elvis, M., & Nicastro, F. 2002, ApJ, 571, 234
Runnoe, J. C., Cales, S., Ruan, J. J., et al. 2016, MNRAS, 455, 1691
Saez, C., Brandt, W. N., Gallagher, S. C., Bauer, F. E., & Garmire, G. P. 2012, ApJ, 759, 42
Sarma, R., Tripathi, S., Misra, R., et al. 2015, MNRAS, 448, 1541
Scott, A. E., Brandt, W. N., Miller, B. P., Luo, B., & Gallagher, S. C. 2015, ApJ, 806, 210
Shemmer, O., Brandt, W., Paolillo, M., et al. 2014, ApJ, 783, 116 (S14)
Silverman, J. D., Mainieri, V., Salvato, M., et al. 2010, ApJS, 191, 124
Sobolewska, M. A., & Papadakis, I. E. 2009, MNRAS, 399, 1597
Stark, A. A., Gammie, C. F., Wilson, R. W., et al. 1992, ApJS, 79, 77
Strotjohann, N. L., Saxton, R. D., Starling, R. L. C., et al. 2016, arXiv:1605.02749
Szokoly, G. P., Bergeron, J., Hasinger, G., et al. 2004, ApJS, 155, 271
Torricelli-Ciamponi, G., Pietrini, P., Risaliti, G., & Salvati, M. 2014, MNRAS, 442, 2116
Tozzi, P., Gilli, R., Mainieri, V., et al. 2006, A&A, 451, 457
Tozzi, P., Mainieri, V., Rosati, P., et al. 2009, ApJ, 698, 740
Treister, E., Virani, S., Gawiser, E., et al. 2009, ApJ, 693, 1713
Turner, T. J., George, I. M., Nandra, K., & Mushotzky, R. F. 1997, ApJS, 113, 23
Turner, T. J., George, I. M., Nandra, K., & Turcan, D. 1999, ApJ, 524, 667
Ueda, Y., Akiyama, M., Hasinger, G., Miyaji, T., & Watson, M. G. 2014, ApJ, 786, 104
Ulrich, M.-H., Maraschi, L., & Urry, C. M. 1997, ARA&A, 35, 445
Uttley, P., McHardy, I. M., & Papadakis, I. E. 2002, MNRAS, 332, 231

Vanden Berk, D. E., Wilhite, B. C., Kron, R. G., et al. 2004, ApJ, 601, 692
Vaughan, S., Edelson, R., Warwick, R. S., & Uttley, P. 2003, MNRAS, 345, 1271
Wang, W.-H., Cowie, L. L., Barger, A. J., Keenan, R. C., & Ting, H.-C. 2010, ApJS, 187, 251
Wilkes, B. 2015, ChNew, 22, 12
Xue, Y. Q., Luo, B., Brandt, W. N., et al. 2011, ApJS, 195, 10
Xue, Y. Q., Luo, B., Brandt, W. N., et al. 2016, ApJS, 224, 15
Yang, Q.-X., Xie, F.-G., Yuan, F., et al. 2015, MNRAS, 447, 1692
York, D. G., Adelman, J., Anderson, J. E., Jr., et al. 2000, AJ, 120, 1579
Young, M., Brandt, W. N., Xue, Y. Q., et al. 2012, ApJ, 748, 124
Zhang, Y.-H. 2011, ApJ, 726, 21
Zoghbi, A., Fabian, A. C., Reynolds, C. S., & Cackett, E. M. 2012, MNRAS, 422, 129